1. Introduction

Nickel–base alloys used as construction material in pressurized water reactors (PWRs) have experienced primary water stress corrosion cracking (PWSCC). Such cracking has occurred in Alloy 600 and Alloy 182/82 components such as steam generator tubes, heater thermal sleeves and penetrations in the pressurizer, penetrations for the control rod drive mechanisms (CRDMs) in reactor pressure vessel head, bottom–mounted instrumentation nozzles, and dissimilar metal welds between the low–alloy steel reactor vessel nozzle and stainless steel (SS) safe–end or pipe. Initiation of PWSCC involves a significant incubation period that depends primarily on temperature and material susceptibility. In general, cracking has occurred much earlier in the Alloy 600 base metal than in the Alloy 182 and Alloy 82 welds and at higher temperature locations within the reactor coolant system. Also, small bore pipes and tubes have cracked earlier than larger size components.

The PWSCC of Alloy 600 steam generator tubes in PWRs has been studied intensively.[1–3] In general, cracking occurs in regions of high residual stress due to cold work, such as the tube roll transition zone (RTZ), U–bends, tube denting locations, and plugs and sleeves.[4–6] The RTZ at the top of the tube sheet is the most common location for such cracking, and the cracks are most frequently axial, although circumferential cracks also occur. PWSCC at U–bends is associated with high residual stresses from the bending process. The use of more resistant materials and improved thermal processing has greatly reduced the incidence of this cracking. PWSCC at dented tube support plates was also related to the presence of residual stresses caused by the denting phenomenon, and the problem has largely disappeared with the resolution of the denting problem. Tube plugs, which typically have high residual stresses, are themselves prone to PWSCC. Heats of Alloy 600 show a wide variability in their susceptibility to PWSCC.[7–9]

The earliest location of PWSCC in components other than the steam generator tubes have been in the base metal of instrument nozzles and heater thermal sleeves in the pressurizer.[10] In these cases, the cracks were always axial and occurred at locations at the highest temperature and in materials with yield strength as low as ≈240 MPa (≈35 ksi), which is the minimum value allowed.

The other major locations of PWSCC of Alloy 600 components are at the nozzle penetrations for the CRDM in the reactor vessel closure heads.[11] In the fall of 1991, during an over–pressurization test, a leak was discovered in the CRDM nozzle at the Bugey 3 plant in France. Metallurgical evaluations indicated that the leak was caused by PWSCC.[12] The main crack had initiated in Alloy 600 base metal and propagated into the Alloy 182 weld metal. Subsequent inspections of CRDM penetrations in the early 1990s in foreign PWRs indicated that ≈6.5% of the nozzles in French plants had axial cracks on the nozzle inner surface, while only ≈1.25% of the nozzles that were inspected in other plants had axial cracks. Inspection of the CRDM nozzles in seven plants in the United States (Point Beach 1, Oconee 2, Cook 2, Palisades, North Anna 1, Millstone 2, and Ginna) at this time suggested that the cracking was much less frequent than in the French plants. None of the cracks found in U.S. plants was through–wall, and until late 2000, no more leaks were found in pressure–vessel head penetrations.

In November 2000, leaks from axial through–wall cracks were identified at Oconee Unit 1, and in February 2001, at Arkansas Nuclear One Unit 1.[13] During the next 15 months, inspections at Oconee Units 2 and 3 and follow–up inspection at Unit 1 identified both axial and circumferential cracks in reactor vessel head penetrations.[14] The presence of circumferential cracks, in particular, raised concerns regarding structural integrity.[15,16] Also, in October 2000, significant boron deposits were discovered near the Loop "A" reactor vessel nozzle to the hot–leg reactor coolant pipe weld at the V.C. Summer

plant.[17] Ultrasonic inspection of the pipe revealed an axial crack and a short, intersecting circumferential crack in the dissimilar metal weld at the top of the pipe. The failed region was repaired using a new SS spool piece and Alloy 152 weld filler metal. Earlier in 2000, two shallow axial flaws had been found in the outlet nozzle–to–safe–end weld of Ringhals Unit 3, and four axial indications were found in the same region of Ringhals Unit 4, in Sweden.[18] Cracks have also been found in pressure–vessel head penetrations at North Anna Unit 2,[19] the Davis–Besse nuclear power plant,[20] and more recently, in the bottom–mounted instrumentation nozzles at South Texas Unit 1.[21,22]

Other instances of PWSCC in components fabricated from Ni alloys include cracking of the nozzle-coupling-to-vessel weld at the steam-generator lower head bowl drain, observed at Catawba Unit 2 in 2001,[23] and cracking in the heat-affected zone of an Alloy 600 safe end in a power-operated relief valve, near the connection to the pressurizer at the Palisades nuclear plant in 1993.[24]

In some incidents of PWSCC, e.g., cracking of the CRDM nozzle at the Davis–Besse plant,[20] leakage of the primary coolant resulted in significant degradation of ferritic steel components. At Davis–Besse, downstream of nozzle #3, a triangular cavity, about 127 mm (50 in.) wide and 178 mm (70 in.) long, had penetrated completely through the thickness of the low–alloy steel reactor pressure–vessel head, leaving only a layer of SS cladding. Damage of this magnitude to the reactor pressure–vessel–head from a leaking CRDM nozzle had not been anticipated. It is important to determine whether the crack growth in the leaking nozzle at Davis-Besse leading to high leak rates is consistent with our understanding of crack growth rates (CGRs) in these materials.

Long–term plant operating experience indicates that PWSCC appears to occur more frequently in wrought Ni–base Alloy 600 components than in the weld metal Alloys 82 and 182 used with Alloy 600. However, in laboratory tests in PWR coolant environments, the SCC susceptibility of Alloy 182 is usually found to be greater than that of Alloy 600, while that of Alloy 82 is comparable to Alloy 600. This apparent inconsistency between field and laboratory experience is an issue that needs further investigation.

Research is being conducted at Argonne National Laboratory (ANL) to evaluate the resistance of Ni alloys and their welds to environmentally assisted cracking in simulated light water reactor (LWR) coolant environments. Existing CGR data for Ni alloys under cyclic and constant loads have been analyzed to establish the effects of key parameters on CGRs.[25–29] Fatigue data in air were analyzed to develop correlations for estimating the fatigue CGRs of Alloys 600 and 690 as a function of the stress intensity factor range ΔK, load ratio R, and temperature.[30] In air, the CGRs of these materials are relatively insensitive to changes in the test frequency. The CGR (da/dN in m/cycle) of Alloy 600 in air is best expressed as

$$da/dN = C_{A600} (1 - 0.82\ R)^{-2.2} (\Delta K)^{4.1}, \quad (1)$$

where ΔK is in $MPa \cdot m^{1/2}$, and C_{A600} is a third-order polynomial in temperature T (°C),

$$C_{A600} = 4.835 \times 10^{-14} + (1.622 \times 10^{-16})T - (1.490 \times 10^{-18})T^2 + (4.355 \times 10^{-21})T^3. \quad (2)$$

In high–dissolved–oxygen (DO) water, the CGRs of Alloy 600 show frequency–dependent enhancement under cyclic loading conditions. In high-DO water, simulating boiling water reactor (BWR) coolant, the environmental enhancement of the growth rates does not appear to depend strongly on the material condition. In contrast, environmental enhancement of CGRs of Alloy 600 in low–DO water does seem to be strongly dependent on material conditions. In the literature[31–35] such variability has been

attributed to thermomechanically controlled parameters such as yield strength and grain boundary coverage of carbides, although the evidence for this dependence is more substantial for steam generator tubing than for structural components.

In earlier ANL work, correlations were developed to estimate the enhancement of CGRs in LWR environments relative to the CGRs in air under the same loading conditions. The best–fit curve for Alloy 600, either in the solution annealed (SA) condition or the SA plus thermally treated condition, in ≈300 ppb DO water is given by the expression[27]

$$CGR_{env} = CGR_{air} + 4.4 \times 10^{-7} (CGR_{air})^{0.33}. \quad (3)$$

As noted, in PWR environments some materials show little enhancement, while others show enhancement at 320°C comparable to that predicted by Eq. 3. Frequency–dependent environmental enhancement is usually associated with susceptibility to SCC under constant loading conditions, e.g., materials with high SCC growth rates exhibit high fatigue CGRs also.

The SCC data for Alloy 600 have been reviewed to determine the effects of critical parameters such as stress intensity factor, temperature, material heat treatment, cold work, and water chemistry on growth rates.[36] The CGR (m/s) under SCC conditions is represented by the correlation,

$$CGR_{A600} = \alpha \exp\left[-\frac{Q}{R}\left(\frac{1}{T} - \frac{1}{T_{ref}}\right)\right](K - K_{th})^{\beta}, \quad (4)$$

where:
- Q = activation energy for crack growth,
  - = 130 kJ/mol (31.1 kcal/mol) for Alloy 600,
- R = universal gas constant,
  - = 8.314×10^{-3} kJ/mol·K (1.103×10^{-3} kcal/mol·°R),
- T = absolute operating temperature in K (or °R),
  - = absolute reference temperature used to normalize the CGR data,
  - = 598 K (1076.67°R),
- α = crack growth amplitude (2.67×10^{-12} at 325°C),,
- K = crack tip stress intensity factor (MPa $m^{1/2}$),
- K_{th} = crack tip stress intensity factor threshold (9 MPa $m^{1/2}$), and
- β = exponent 1.16.

The effect of the stress intensity factor (K) on SCC crack growth for Ni–alloy welds in PWR environments has been represented by a modified[37] version of the above relationship between CGR_{env} (m/s) and stress intensity factor K (MPa $m^{1/2}$). However, unlike the CGR relationship for Alloy 600, the CGR relationship for Ni–alloy welds has no threshold value for the stress intensity factor K,

$$CGR_{Ni\ weld} = \alpha \exp\left[-\frac{Q}{R}\left(\frac{1}{T} - \frac{1}{T_{ref}}\right)\right](K)^{\beta}, \quad (5)$$

where Q, R, T, and T_{ref} are the same as in Eq. 4, crack growth amplitude α is 1.5×10^{-12} at 325°C, and exponent β is 1.6.

The objective of this report is to determine whether the crack growth in materials from the CRDM nozzle and the J–groove weld of the Davis–Besse plant and the hot–leg reactor vessel nozzle-to-pipe weld from the V.C. Summer alpha loop, are consistent with our understanding of CGRs in these materials. Crack growth rates have been obtained in a simulated PWR environment on Alloy 600 removed from the Davis–Besse CRDM nozzle #3, and Alloy 182 from nozzle #11 J–groove weld, as well as on Alloys 82 and 182 from the "A" hot–leg nozzle–to–pipe weld from the V.C. Summer reactor coolant system. Crack growth tests were conducted on 1/4–T or 1/2–T compact tension (CT) specimens under cyclic loading using a sawtooth waveform with 30–1000 s rise times and at constant load with or without periodic partial unloading. The tests were performed at 316°C (600°F) for the Davis–Besse alloys and at 320°C for the V.C. Summer alloys. Crack extension was monitored by DC potential measurements. The results are compared with the existing CGR data for Alloys 600 and 182 and 82 to determine the relative susceptibility of these materials to PWSCC. The results of a detailed metallographic examination of the alloys to characterize their microstructure and fracture morphology are also presented.

2 Experimental

2.1 Materials

2.1.1 Davis-Besse CRDM Nozzle and J–Groove Weld

Two alloy samples from the Davis-Besse (D–B) reactor pressure vessel head were received from BWXT Technologies, Inc., in Lynchburg, Virginia. The samples include a 63.5–mm (2.5–in.) long ring from Nozzle #3 (Fig. 1) and piece D2, which contains a large portion of the J–groove weld from Nozzle #11 (Fig. 2a). The nozzle ring was produced at BWXT Technologies from two transverse cuts made through the nozzle at 25.4 and 88.9 mm (1.0 and 3.5 in.) from the bottom of the nozzle (near the J–groove weld end). It is estimated that ≈114.3 mm (4.5 in.) of the nozzle end was bored away during the removal process at the Davis–Besse site. Piece D2 with the J–groove weld from Nozzle #11 resulted from four cuts made at BWXT Technologies. Cuts #1–3 are shown in Fig. 2b, and Cut #4, ≈25.4 mm (≈1.0 in.) above the J–groove weld, is shown in Fig. 2a.

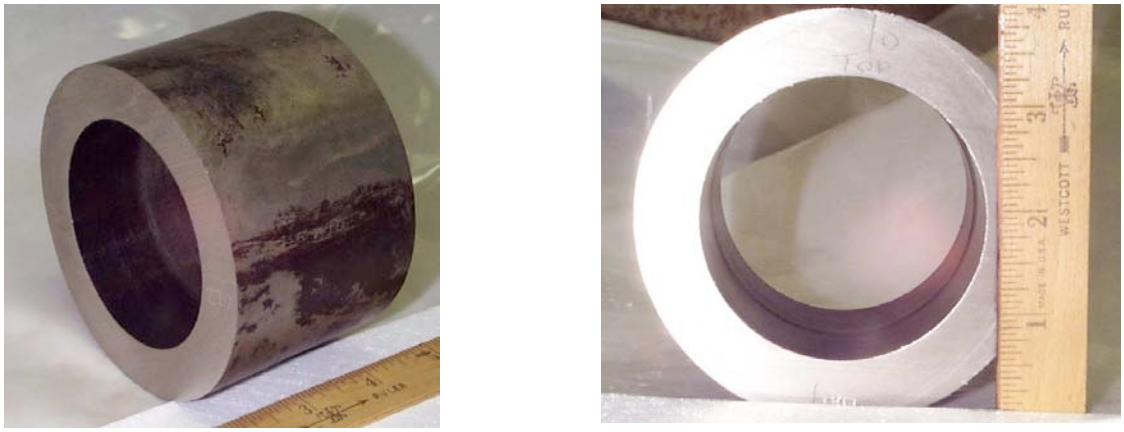

Figure 1. Photographs of the ring from Davis–Besse CRDM Nozzle #3.

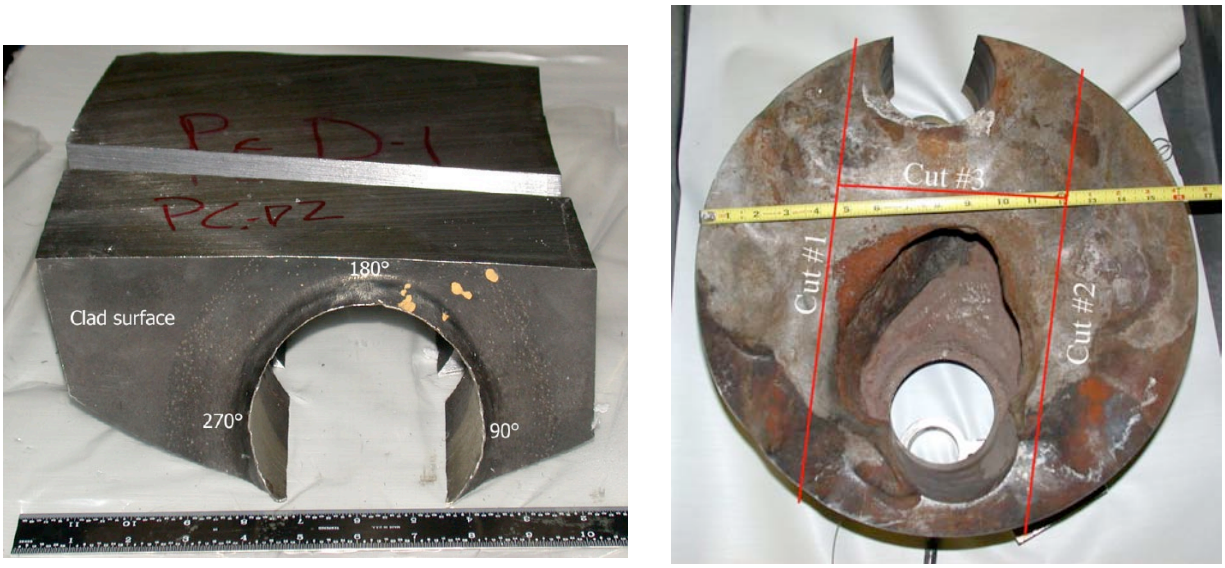

Figure 2. Photographs of (a) the ring from Davis–Besse CRDM Nozzle #3 and (b) reactor pressure vessel head sample with J–groove weld from Nozzle #11 (piece D2).

In the original Davis–Besse reactor upper head, CRDM Nozzles #1–5 were fabricated from Alloy 600 seamless tubing per American Society of Mechanical Engineers (ASME) SB–167 (Heat M3935). The final mill anneal temperature is estimated to be 871–927°C (1600–1700°F). The mill–certified chemical composition and room–temperature tensile properties are given in Table 1.

Table 1. Chemical composition (wt.%) and tensile properties of Alloy 600 (Heat M3935) from Davis–Besse CRDM Nozzle #3.

	C	Mn	Fe	P	S	Si	Cu	Ni	Cr	Co	Ti
Specification	0.15 max	1.0 max	6.0 – 10.0	–	0.015 max	0.5 max	0.50 max	72 min	14.0 – 17.0	–	–
Vendor	0.028	0.27	6.25	0.004	0.002	0.37	0.01	77.89	15.58	0.01	–
ANL	0.030	0.24	5.93	<0.05	0.003	0.47	<0.03	72.10	15.25	0.04	0.25
	Yield Strength, MPa (ksi)				Tensile Strength, MPa (ksi)				Elongation, %		
	334 (48.5)				590 (85.6)				60		

The CRDM nozzle counterbores were machined in the A533 Gr.–B Cl 1 low–alloy steel reactor vessel head, which was previously clad with Type 308 SS. The CRDM J–groove weld preparations were then ground into the reactor pressure vessel head. After grinding, the J–groove preparations were buttered with Alloy 182 (E–NiCrFe–3) by manual metal arc welding. The reactor vessel head was then stress relieved for 8 h at 607 ± 22°C (1125 ± 40°F). Each Alloy 600 nozzle was custom ground for a diametrical interference fit of 0.0254–0.0533 mm (0.0010–0.0021 in.) with the CRDM penetrations in the reactor vessel head. Each nozzle was attached to the reactor vessel head by a partial penetration weld (J–groove) using Alloy 182 filler metal. On the basis of American Society for Testing and Materials (ASTM) specifications, the chemical composition and minimum tensile properties of the as–welded Alloy 182 are given in Table 2. The welds did not receive any post–weld heat treatment. The temperature near the J–groove weld locations is estimated to be ≈318°C (605°F) during operation.

Table 2. Chemical composition (wt.%) and tensile properties of Alloy 182 from Davis–Besse CRDM Nozzle #11 J–groove weld.

	C	Mn	Fe	S	Si	Cu	Ni	Cr	Ti	Nb	Co
Specification	0.10 max	5.0 – 9.5	6.0 – 10.0	0.015 max	1.0 max	0.50 max	Bal	13.0 – 17.0	1.0 max	1.0 – 2.5	0.12 max
ANL	0.045	7.38	7.64	0.017	0.52	<0.04	Bal	13.5	0.27	1.81	0.04
	Yield Strength, MPa (ksi)				Tensile Strength, MPa (ksi)				Elongation (%)		
	310.3 (45.0)				551.6 (80.0)				30		

2.1.2 V.C. Summer Reactor Vessel Nozzle–to–Pipe Weld

A portion of a spool piece was obtained from the "A" loop hot leg of the V.C. Summer plant. The piece is 152 mm (6 in.) × 229 mm (9 in.) and 64 mm (2.5 in.) thick and includes the reactor vessel nozzle–to–pipe dissimilar metal weld. Figure 3 presents photographs of the piece showing the cross section through the weld (Fig. 3a) and the 229-mm (9-in.) long arc of the pipe (Fig. 3b). In Fig. 3a, the low–alloy steel nozzle section is on the left (dark grey), and the pipe is on the right. The nozzle has ≈10 mm (0.39 in.) Alloy 182 cladding on the inner surface (Fig. 3a top left surface).

A schematic of the "A" hot–leg nozzle–to–pipe weld in the V.C. Summer reactor coolant system is shown in Fig. 4. The V.C. Summer reactor began service in 1983. The reactor vessel was fabricated by Chicago Bridge and Iron Company. The reactor vessel nozzle is a A508 Class 2 low–alloy steel forging,

which was buttered with Alloy 182 weld metal before heat treatment. The main loop piping is a forged A 376 Type 304N SS. The weld between the nozzle and the main loop piping was made in the field using Alloy 82 weld metal. The chemical composition and minimum tensile properties of the as–welded Alloy 82 and Alloy 182 from the V.C. Summer nozzle–to–pipe weld are given in Tables 3 and 4, respectively. The normal hot leg operating temperature is 326°C (619°F).

(a) (b)

Figure 3. Photographs of the V.C. Summer spool piece.

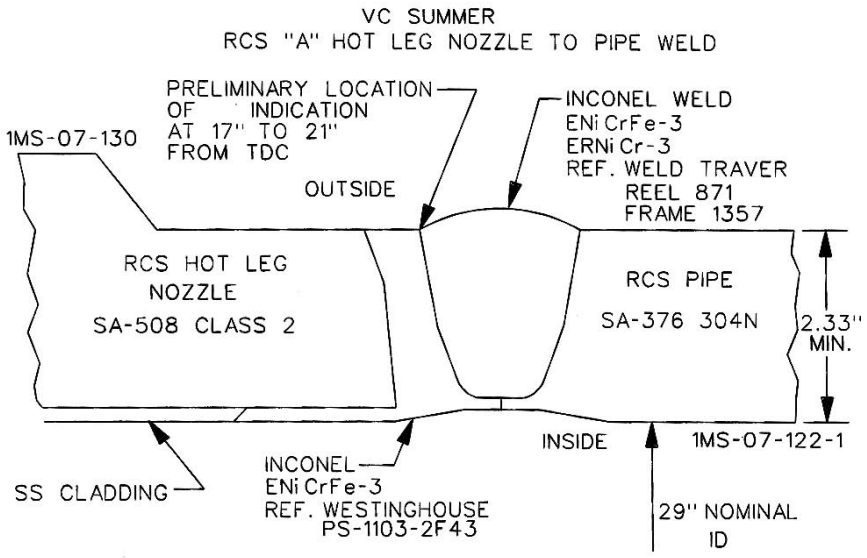

Figure 4. Schematic diagram of the V.C. Summer hot–leg nozzle–to–pipe weld in the reactor coolant system.

Table 3. Chemical composition (wt.%) and tensile properties of Alloy 82 weld metal from the V.C. Summer hot–leg nozzle–to–pipe weld.

	C	Mn	Fe	S	Si	Cu	Ni	Cr	Ti	Nb	Co
Specification	0.10 max	2.5 – 3.5	3.0 max	0.015 max	0.50 max	0.50 max	Bal	18.0 – 22.0	0.75 max	2.0 – 3.0	0.75 max
ANL	0.038	2.87	2.76	0.001	0.18	0.19	Bal	18.6	0.44	2.51	0.04
	Yield Strength, MPa (ksi)				Tensile Strength, MPa (ksi)				Elongation (%)		
	310.3 (45.0)				551.6 (80.0)				30		

Table 4. Chemical composition (wt.%) and tensile properties of Alloy 182 butter from the V.C. Summer hot–leg nozzle–to–pipe weld.

	C	Mn	Fe	S	Si	Cu	Ni	Cr	Ti	Nb	Co
Specification	0.10 max	5.0 – 9.5	6.0 – 10.0	0.015 max	1.0 max	0.50 max	Bal	13.0 – 17.0	1.0 max	1.0 – 2.5	0.12 max
ANL	0.049	7.09	7.94	0.010	0.66	0.10	Bal	14.4	0.72	1.62	0.05
	Yield Strength, MPa (ksi)				Tensile Strength, MPa (ksi)				Elongation (%)		
	310.3 (40.0)				551.6 (80.0)				30		

2.2 Specimen Geometry

Cylindrical–tensile, 6–mm– (0.24–in.–) thick 1/4–T CT, and 9–mm– (0.35–in.–) thick 1/2–T CT, specimens were machined from the Davis–Besse CRDM nozzle and J–groove weld and V.C. Summer nozzle–to–pipe weld and butter. The configurations of the 1/2–T CT and 1/4–T CT specimens are shown in Fig. 5, and those of the cylindrical–tensile specimens with 20.3–mm (0.8–in.) or 12.7–mm (0.5–in.) gauge length are shown in Fig. 6.

2.2.1 Davis–Besse Alloys

The orientation and location of the specimens from the Davis–Besse material are shown in Fig. 7. A thin surface layer was machined from the inner diameter (ID) and outer diameter (OD) of the nozzle ring and from the cladding of the J–groove weld to decrease the surface activity to an acceptable level. Tensile specimens were obtained in both longitudinal (L) and circumferential (C) orientations for the J–groove weld, but only in the longitudinal orientation for the nozzle. Because of insufficient height of the weld, subsize tensile specimens [i.e., 12.7–mm (0.5–in.) gauge] were machined in the L orientation from the J–groove weld to ensure that the entire gauge length consisted of the weld metal alone. For the nozzle and J–groove weld materials, both 1/4–T and 1/2–T CT specimens were obtained in L and C orientations (i.e., corresponding to circumferential and axial crack, respectively). For the C orientation, the direction normal to the fracture plane is in the C direction, and the crack growth is in the L direction, and vice versa for the L orientation. A radiological survey of the machined tensile and CT specimens indicated <0.1 mR/h βγ on contact and no loose activity.

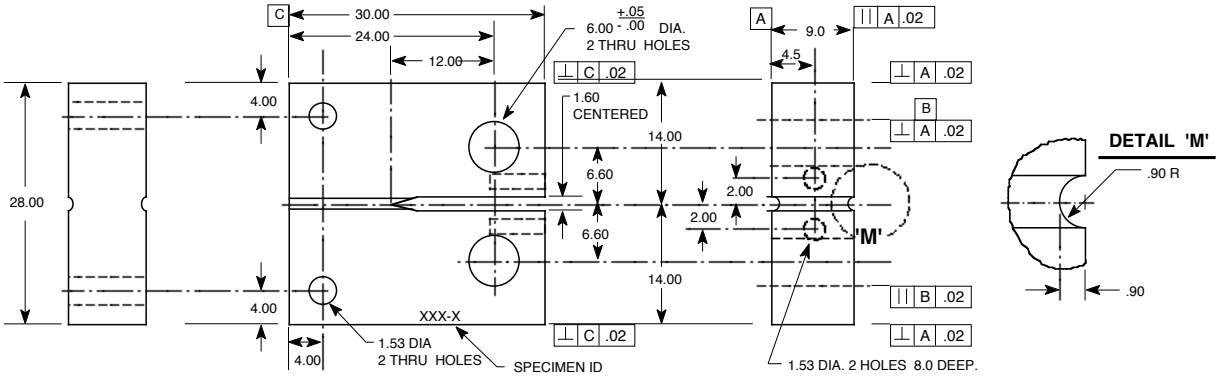

(a)

Figure 5. Configurations of the (a) 1/2–T and (b) 1/4–T compact tension specimen.

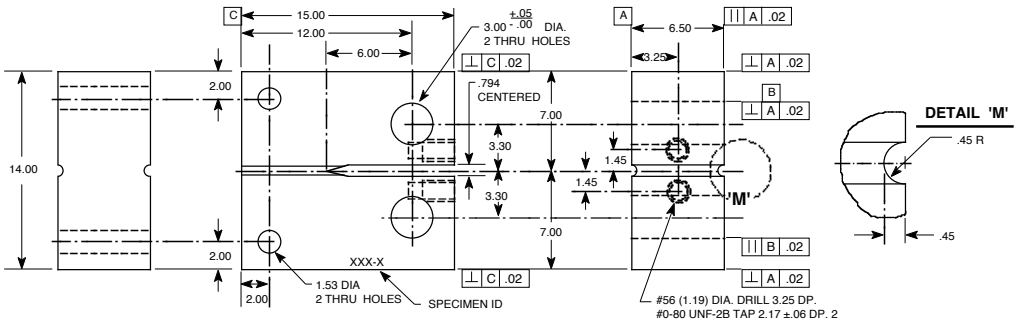

(b)

Figure 5. (Contd.)

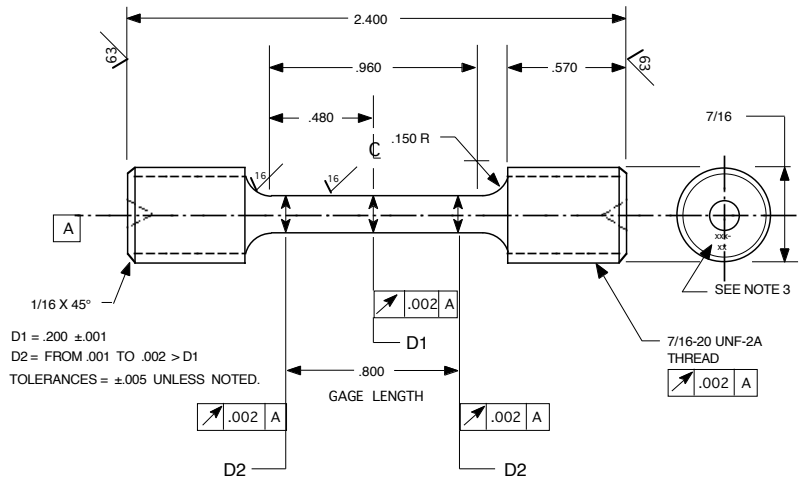

(a)

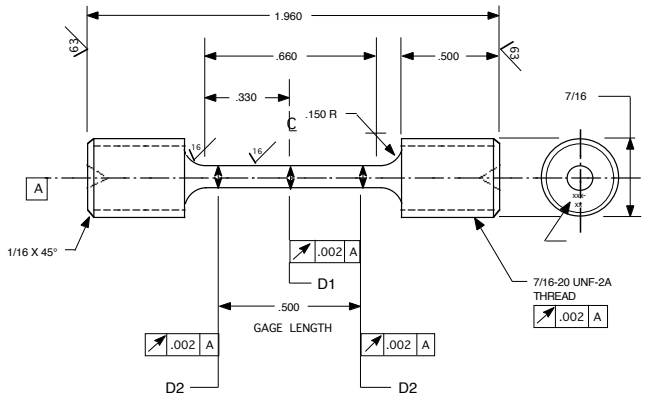

(b)

Figure 6. Configurations of the tensile specimen with a (a) 20.3-mm and a (b) 12.7-mm gauge length.

During cutting and fabrication of specimens from the Davis–Besse J–groove weld of Nozzle #11, several structural defects were uncovered. In nearly all cases, the flaws appeared to be caused by lack of fusion and contained inclusions. A schematic of the J–groove weld sample showing the location of the flaws is presented in Fig. 8; locations of the defects are marked on the picture of piece D2 of the J–groove weld in Fig. 9. Most of the defects appeared to be between the reactor vessel head butter and the J–groove weld. A significant number of the weld specimens had to be discarded because of these defects.

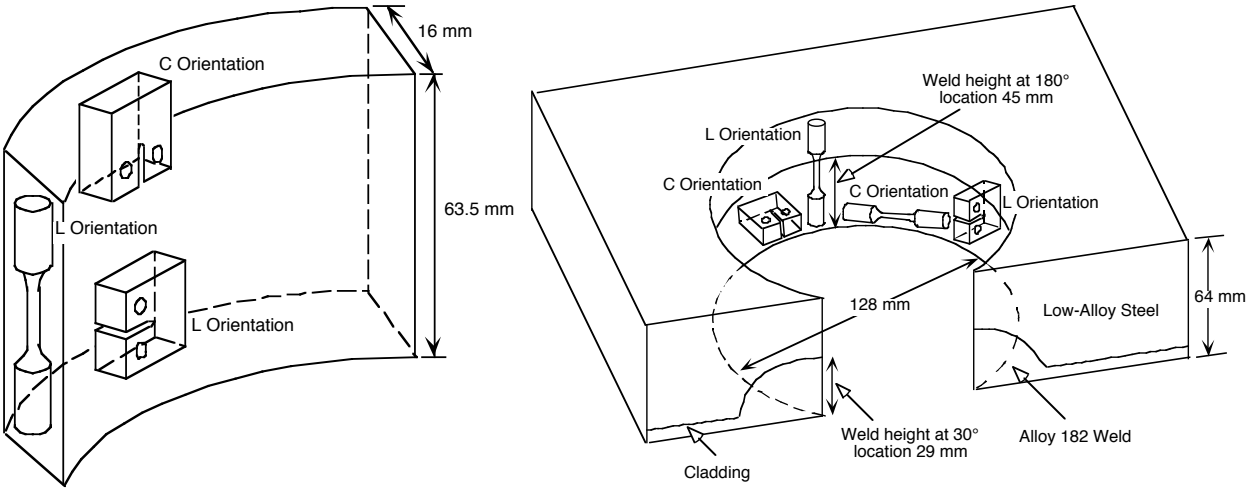

(a) (b)

Figure 7. Orientation and location of the mechanical–test specimens obtained from Davis–Besse (a) CRDM Nozzle #3 and the (b) J–groove weld of Nozzle #11.

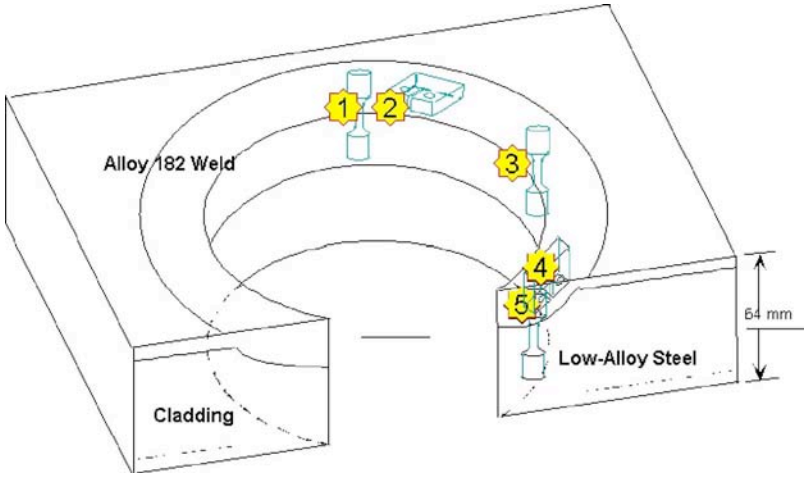

Figure 8. Orientation and location of the mechanical–test specimens from the J–groove weld of Nozzle #11 on which defects were found during fabrication.

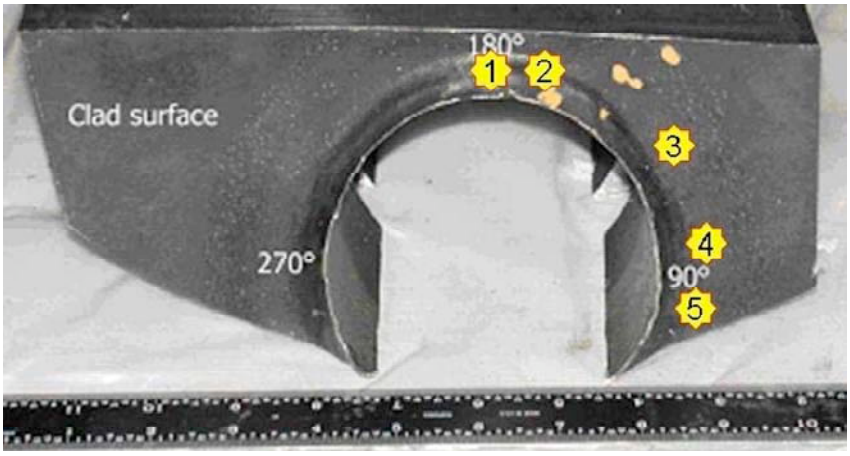

Figure 9. Approximate locations where defects were found during fabrication of test specimens from CRDM Nozzle #11 J–groove weld.

A defect in the tensile Specimen J11TL-4, taken from location "1" in Fig. 9, was detected only after the tensile test was completed, and a significant loss of ductility was observed. The fracture surface of this sample is shown in Fig. 10, where a large inclusion is indicated by an arrow. In a CT specimen machined from material taken from location "2" in Fig. 9, a defect was found during machining. Figure 11 shows structural defects on the face and side surface of specimen blanks used for machining CT specimens; the flaws are indicated by an arrow. The approximate cross–sectional dimensions of these defects were 2.5 × 1 mm and 3.5 × 1.5 mm (0.10 × 0.04 in. and 0.14 × 0.06 in.); the depth was 0.5 mm (0.02 in.) for both defects.

Similar defects were found during machining of tensile specimens from locations "3" and "5" and the 1/4–T CT specimen from location "4." The defect at location "3", 1.5 × 0.5 × 0.5 mm (0.06 × 0.02 × 0.02 in.) in size, could be completely removed during machining of the specimen without affecting the integrity. The defect sizes at locations "4" and "5" were 1.5 × 1.5 × 0.6 mm and 3 × 1 × 0.2 mm (0.06 × 0.06 × 0.024 in. and 0.12 × 0.04 × 0.008 in.), respectively.

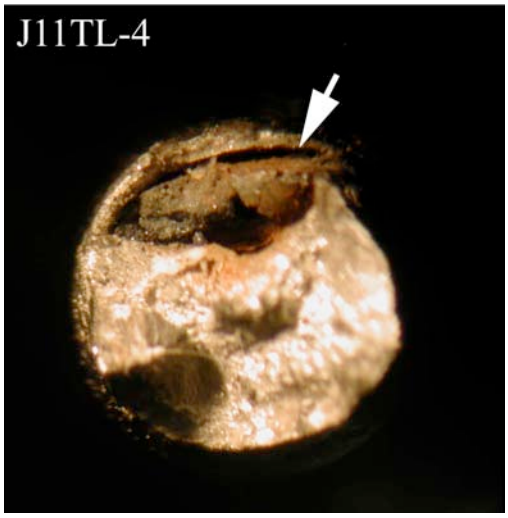

Figure 10.
Large defect (inclusion) found on the fracture surface of tensile Specimen J11TL-4, the cause of a significant loss of ductility.

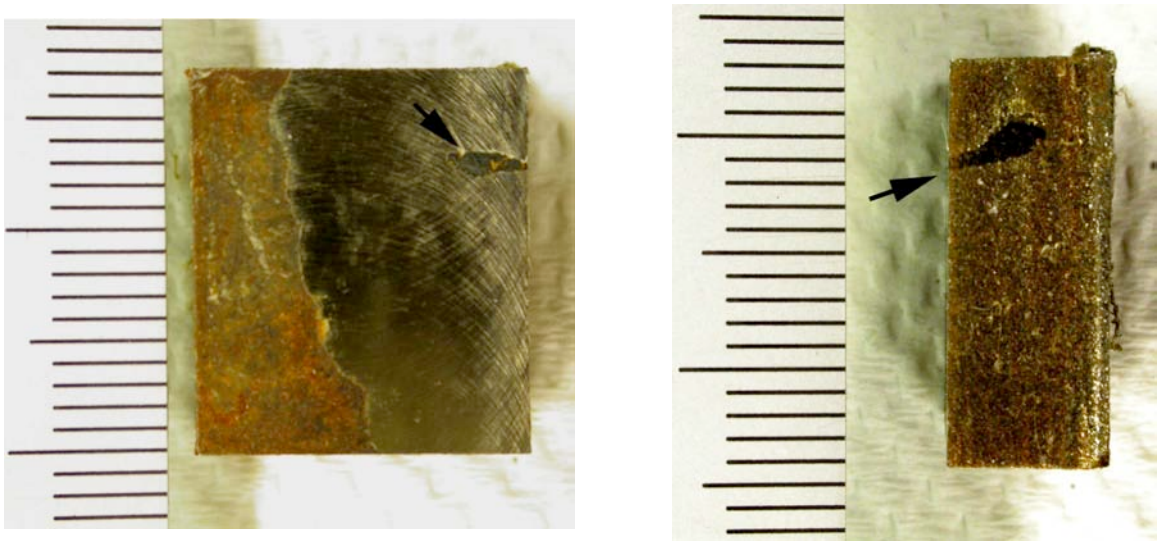

(a) (b)

Figure 11. Structural defects on the (a) face and (b) side surface of the specimen blanks used for machining CT specimens.

2.2.2 V.C. Summer Alloys

The locations and orientations of the tensile bars from both the butter and weld regions are shown in Figs. 12a and 12b for both the C and L orientations. In the C orientation, the sample designations are WTC and BTC for the weld and buttered regions, respectively. Similarly, in the L orientation, the sample designations are WTL and BTL. The locations and orientations of the CT specimens are shown in Figs. 13a and 13b for R (radial) and L orientations, respectively. In the "R" orientation, the sample designations are WCR and BCR for the weld and buttered regions, respectively. Similarly, in the L orientation, the sample designations are WCL and BCL. Only 9–mm– (0.35–in.–) thick 1/2–T CT specimens were obtained from the V.C. Summer material.

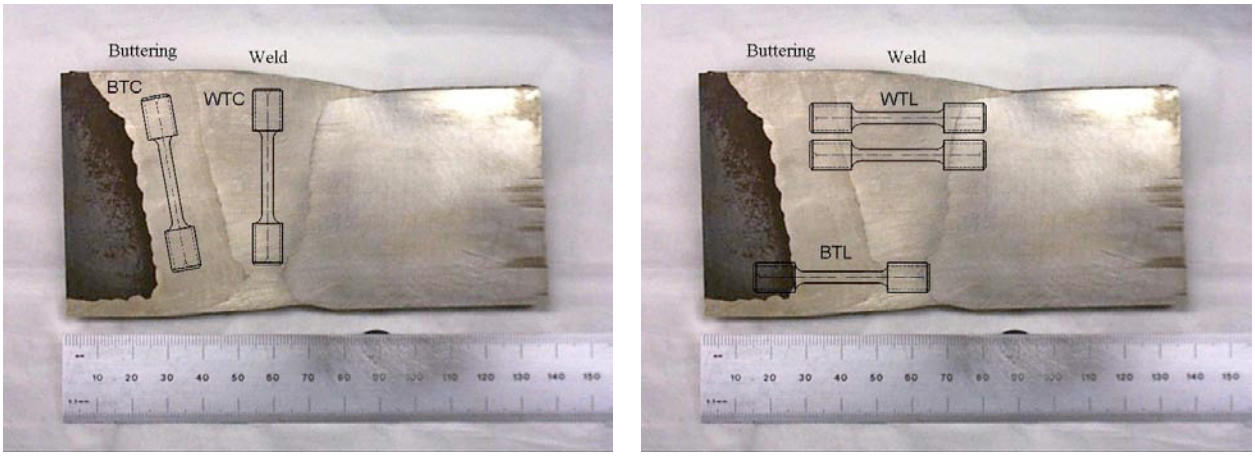

(a) (b)

Figure 12. Schematic of the tensile specimens fabricated from the V.C. Summer weld piece for (a) "C" and (b) "L" orientations.

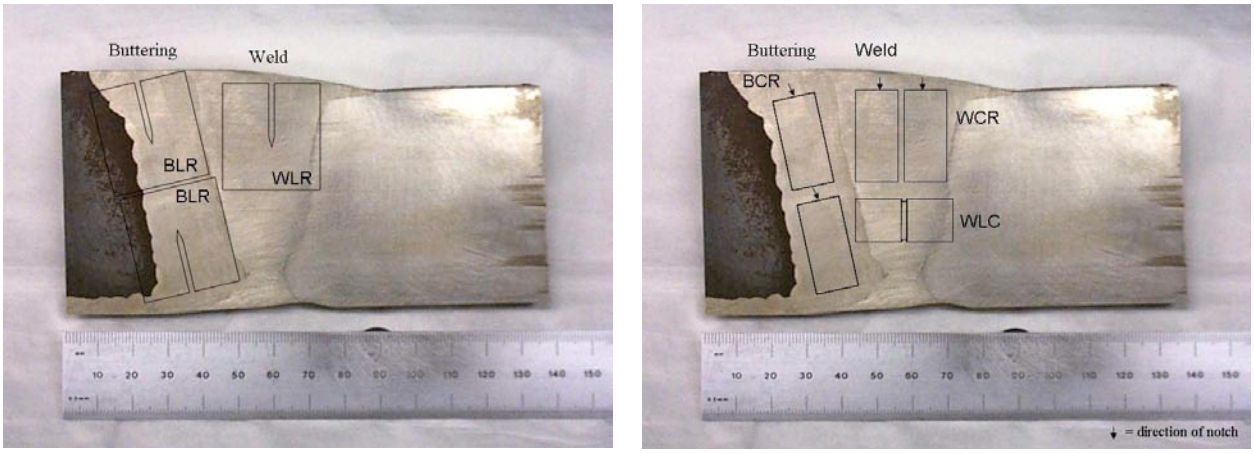

(a) (b)

Figure 13. Schematic of the CT specimens fabricated from the V.C. Summer weld piece for (a) "L" and (b) "C" orientations.

Prior to machining, the V.C. Summer spool piece was surveyed at two spots each along the weld, nozzle section, and the pipe; the results for inner and outer surface are given in Table 5. In general, dose rates are highest on the weld and lowest on the nozzle (note that the inner surface of the nozzle shows a high exposure rate because of the Alloy 182 cladding). Also, the dose rates on the inner surface are slightly higher than those on the outer surface.

Table 5. Radiological survey report for the V.C. Summer spool piece.

	Inner Surface			Outer Surface		
	Weld	Nozzle	Pipe	Weld	Nozzle	Pipe
Beta @ 1 in. (mR/h)	28	15	13	14	6	10
	28	10	12	11	5	10
Gamma @ 1 in. (mR/h)	20	10	13	13	6	10
	17	10	14	11	5	9

2.3 Test Facilities

The CGR tests were conducted in two test facilities. Tests on the Davis–Besse materials were conducted in a CGR test facility with a 1–liter SS autoclave using either 1/4–T or 1/2–T CT specimens; tests on the V.C. Summer materials were conducted in a CGR test facility with a 6–liter SS autoclave using 1/2–T CT specimens. A detailed description of the two facilities is given below.

2.3.1 CGR Test Facility with a 1–Liter Autoclave

The 1–liter autoclave test facility is a modified version of the in–cell facility for conducting CGR tests on irradiated materials. The actuator assembly [hydraulic actuator, 22–kN (5–kip) load cell, autoclave cover plate, and the internal specimen load train] and the furnace are mounted on top of a portable wheeled cart that can be easily relocated. A 1–liter SS autoclave is installed inside the furnace for conducting tests in simulated PWR environments. The furnace and the autoclave body are mounted on a pneumatic cylinder and can be raised to enclose the internal specimen load train and the specimen during the test. Water is circulated through a port in the autoclave cover plate with concentric piping that serves both as an inlet and outlet.

The 1/4–T or 1/2–T CT specimen is mounted in the clevises with Inconel pins (Fig. 14). The two sets of clevises are at 90º opposition, forming a pair of universal joints. The specimen and clevises are kept electrically insulated from the load train by using oxidized Zircaloy pins and mica washers to connect the clevises to the rest of the load train. The crack length is monitored by reversed-current DC

Figure 14.
Photograph of the specimen load train for the 1–liter autoclave.

potential drop measurements. Platinum wires are used for the current and potential leads. The current leads are attached to SS split pins that are inserted into the holes at the top and bottom of the specimen. The potential leads are attached by screwing short SS pins into threaded holes in the specimen and attaching the platinum wires with in–line SS crimps. An Instron Model 8500+ Dynamic Materials Testing System is used to load the specimen.

A schematic diagram of the recirculating water system is shown in Fig. 15. The recirculating water system consists of a storage tank, high–pressure pump, an accumulator, regenerative heat exchanger, autoclave preheater, autoclave, electrochemical potential (ECP) cell preheater, ECP cell, air–cooled coil, water cooled chill–block, Mity Mite^{TM} back-pressure regulator, and return line to the storage tank. In the recirculating mode, the ECP cell is bypassed and water from the autoclave is returned to the storage tank through the regenerative heat exchanger, water–cooled chill block, and back pressure regulator. With the ECP cell in use, to avoid any possible contamination of chlorides from the reference electrode, the system is operated only in the once-through mode; water from the autoclave is circulated through the ECP cell preheater, ECP cell, air–cooled coil, water–cooled chill block, back–pressure regulator, and drain to the sump (Item 29 in Fig. 15). Water is circulated at flow rates of 45–160 mL/min.

The feedwater storage tank, manufactured by Filpaco Industries, has a 130–liter capacity and is constructed of either Type 304 or 316 SS. The tank is designed for vacuum and over–pressure to 414 kPa (60 psig). The storage tank has a hydrogen cover gas to maintain a desired dissolved hydrogen concentration in the water.

1. COVER GAS SUPPLY TANK
2. HIGH-PRESSURE REGULATOR WITH FLASH ARRESTOR
3. LOW-PRESSURE REGULATOR
4. FLOW METER
5. GAS PURIFIER
6. PRESSURE GAUGE
7. PRESSURE RELIEF VALVE WITH FLASH ARRESTOR
8. VENT TO AIR WITH FLASH ARRESTOR
9. FEEDWATER STORAGE TANK
10. SPARGE TUBE
11. FEEDWATER FILL PORT
12. SOLENOID VALVE
13. HIGH-PRESSURE PUMP
14. CHECK VALVE
15. RUPTURE DISK
16. ACCUMULATOR
17. HIGH-PRESSURE GAUGE
18. REGENERATIVE HEAT EXCHANGER
19. AUTOCLAVE PREHEATER
20. PARR AUTOCLAVE
21. BAL SEAL
22. THERMOCOUPLE WELL
23. ECP CELL PREHEATER
24. ECP CELL
25. ECP CELL BYPASS LINE
26. AIR–COOLED COIL
27. WATER COOLED BLOCK
28. BACK-PRESSURE REGULATOR
29. DRAIN TO SUMP
30. RECIRCULATING PUMP
31. RETURN LINE

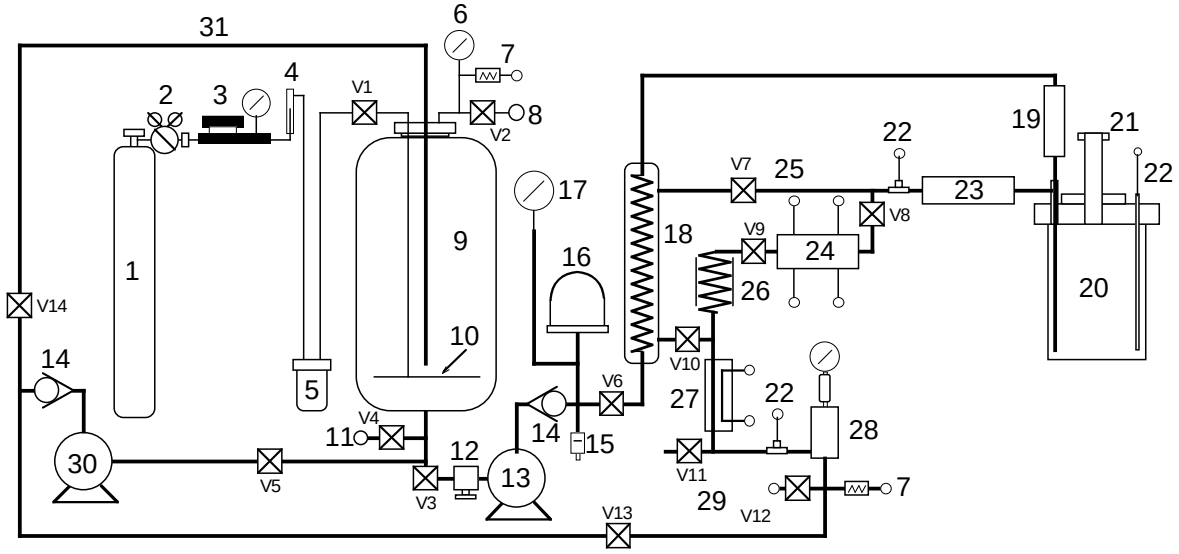

Figure 15. Schematic diagram of the recirculating water system.

The simulated PWR feedwater contains 2 ppm Li, 1000 ppm B, ≈2 ppm dissolved hydrogen (≈23 cm^3/kg), and less than 10 ppb DO. It is prepared from the laboratory supplies of deionized water by first passing this water through a local filtration system that includes a carbon filter, an Organex Q filter, two ion exchangers, and a 0.2–mm capsule filter. The DO in the deionized water is reduced to <10 ppb by bubbling/sparging a mixture of N_2 + 5% H_2 through the water. To speed deoxygenation of a fresh tank of water, a vacuum may be applied to the feedwater tank at the vent port. The PWR water is prepared by dissolving boric acid and lithium hydroxide in 20 liter of deionized water before adding the solution to the supply tank. The hydrogen gas pressure in the feedwater tank is maintained at ≈62 kPa (≈9 psig). The dissolved hydrogen in water is calculated from the tank hydrogen pressure and temperature.

Water samples are taken periodically to measure pH, conductivity, and DO concentration both upstream and downstream from the autoclave. An Orbisphere meter and CHEMetrics™ ampules are used to measure the DO concentrations in the supply and effluent water. The redox and open–circuit corrosion potentials are monitored at the autoclave outlet by measuring the ECPs of platinum and an Alloy 600 electrode individually against a 0.1–M KCl/AgCl/Ag external (cold) reference electrode. The measured ECPs, $E_{(meas)}$ (mV), were converted to the standard hydrogen electrode (SHE) scale, $E_{(SHE)}$ (mV), by the polynomial expression[38]

$$E_{(SHE)} = E_{(meas)} + 286.637 - 1.0032(\Delta T) + 1.7447x10^{-4}(\Delta T)^2 - 3.03004x10^{-6}(\Delta T)^3, \quad (6)$$

where ΔT(°C) is the temperature difference along the electrode compartment in a 0.1–M KCl/AgCl/Ag external reference electrode (i.e., the test temperature minus the ambient temperature).

2.3.2 CGR Test Facility with a 6–Liter Autoclave

The 6–liter autoclave test facility consists of an MTS closed-loop electro–hydraulic material test system equipped with an extended column MTS load frame rated at 89 kN (20,000 lb) maximum. The 5.7–liter Type 316 SS autoclave has a 175–mm (6.875–in.) OD and is rated for a working pressure of 5050 psig (35 MPa) at 343°C (650°F). The load frame is accessorized with an MTS 810 control console, and a hydraulic pump. The autoclave is connected to a recirculating or once–through water system. The test facility also consists of a temperature control unit, a DC potential control console, a DC potential measurement unit, and a data acquisition and recording system. The autoclave, mounted within the load frame, has been modified to permit a ≈19–mm (0.75–in.) diameter shaft to load the test specimen through a "Bal-Seal" gland in the top of the autoclave cover. Up to three 1–T or 1/2–T CT specimens can be tested in series inside the autoclave.

The test facility is designed for easy access to the specimens during assembly of the test train. The actuator assembly, consisting of the hydraulic actuator, load cell, autoclave plug, and the internal specimen load train, may be raised and lowered hydraulically to position the specimens at a convenient height. A photograph of the specimen load train is shown in Fig. 16. A CT specimen may be substituted for any or all of the three central in-line blocks.

The autoclave is continuously supplied with simulated primary water solution from the feedwater tank. Figure 17 shows a schematic diagram of the water system. The water system consists of a feedwater storage tank, high–pressure pump, regenerative heat exchanger, autoclave preheater, test autoclave, ECP cell, back pressure regulator, and return line to the feedwater tank. In the once–through mode, the return line is connected to the drain. Water is circulated at relatively low flow rates, i.e., 15–25 mL/min.

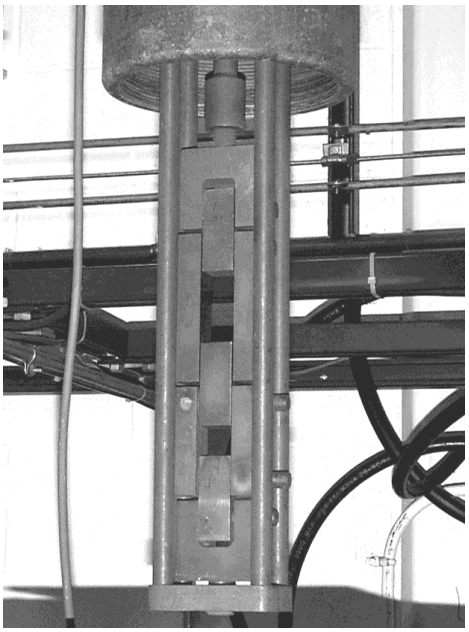

Figure 16.
Photograph of the specimen load train.

1. COVER GAS SUPPLY TANK
2. HIGH-PRESSURE REGULATOR WITH FLASH ARRESTOR
4. LOW-PRESSURE REGULATOR
5. FLOW METER
6. GAS PURIFIER
7. PRESSURE GAUGE
8. PRESSURE RELIEF VALVE WITH FLASH ARRESTOR
9. VENT TO AIR WITH FLASH ARRESTOR
10. FEEDWATER STORAGE TANK
11. SPARGE TUBE
12. FEEDWATER FILL PORT
13. WATER SAMPLE PORT
14. SOLENOID VALVE
15. HIGH-PRESSURE PUMP
16. CHECK VALVE
17. AIR INJECTION PORT
18. SYSTEM BLEED PORT
19. RUPTURE DISK
20. PRESSURE TRANSDUCER
21. HIGH-PRESSURE GAUGE
22. REGENERATIVE HEAT EXCHANGER
23. AUTOCLAVE PREHEATER
24. COMMERCIAL AUTOCLAVE
25. THERMOCOUPLE WELL
26. BAL SEAL RETAINER
27. ECP CELL
28. ECP CELL BYPASS LINE
29. BACK-PRESSURE REGULATOR
30. PRESSURE RELIEF VALVE

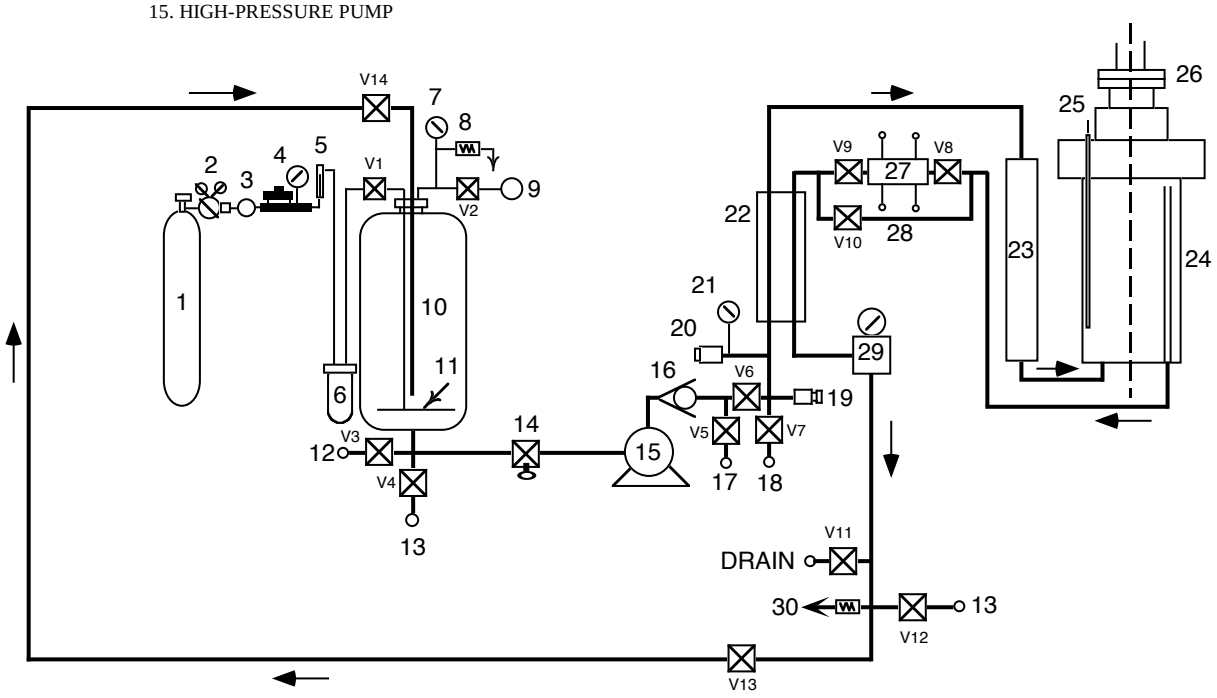

Figure 17. Schematic diagram of the recirculating autoclave system used for CGR tests.

The descriptions of the feedwater supply system and preparation of simulated PWR water are the same as for the 1–liter autoclave test facility.

2.4 Test Procedure

The CGR tests were performed in accordance with ASTM E–647 "Standard Test Method for Measurement of Fatigue Crack Growth Rates" and ASTM E–1681 "Standard Test Method for Determining a Threshold Stress Intensity Factor for Environment–Assisted Cracking of Metallic Materials under Constant Load." The CGR tests were conducted in the load–control mode using a triangular, sawtooth, or trapezoidal waveform with load ratio R of 0.2–0.7. The CT specimens were fatigue precracked in the test environment at load ratio R = 0.2 or 0.3, triangular waveform, frequency of ≈1 Hz, and maximum stress intensity factor K_{max} of 16–25 MPa·$m^{1/2}$. After ≈0.5–mm extension, R was increased incrementally to 0.7, and the loading waveform changed to a slow/fast sawtooth with rise times progressively increasing through a range of 30–1000 s. The SCC growth rates were determined at constant load or with a trapezoidal waveform with R = 0.7, rise time of 12–1000 s, 3600–s hold period at peak, and 12–s unload time. This loading sequence results in confidently reproducible CGRs.[39] During individual test periods, K_{max} was maintained approximately constant by periodic load shedding (less than a 2% decrease in load at any given time).

Crack extensions were monitored by the reversing DC potential difference method. The current leads were attached to the holes on the top and bottom surfaces of the specimen, and potential leads were either welded or attached with a pin to the front face of the specimen. Also, for the tests in the 6–liter autoclave, an Alloy 600 internal reference bar was installed near the test specimen to compensate for the effects of changes in resistivity of the material with time. The CT specimen and reference bar were connected in series, and the DC potential across the specimen as well as the reference bar was monitored continuously during the test. The results for the reference bar were used to normalize potential drop measurements for the CT test specimen. Because of limited space, an internal reference bar could not be used for the tests in the 1–liter autoclave. However, the results of DC potential measurements in a PWR environment indicate that after the initial ≈200 h, the change in resistivity of Ni alloys is insignificant. Consequently, prior to the CGR tests, all specimens were soaked in the test environment for ≈10 days.

The crack length was determined from the DC potential drop measurements using correlations that were developed from a best fit to experimental data for normalized crack length and normalized DC potential. For a 1/2–T CT specimen, the normalized crack length a/W is expressed as

$$\left(\frac{a}{W}\right) = \left[0.2748\left(\frac{U}{U_0} - 0.5\right)\right]^{-0.354}, \tag{7}$$

where W is the specimen width, and U and U_0 are the present and initial potentials across the specimen. At the completion of a test, the final crack size was marked by fatigue cycling in air at room temperature. The specimen was then fractured, and the fracture surfaces were examined by optical or electron microscopy to measure the final crack length using the 9/8 averaging technique (i.e., the two near–surface measurements were averaged, and the resultant value was averaged with the remaining seven measurements). The number of measurements was increased for irregular crack fronts.

The experimental data were consistent with the screening criteria of Ref. 37. All specimens showed 100% engagement (i.e., crack extension occurred over the entire machine notch, and the crack front was relatively straight). Also, under environmentally enhanced conditions, fracture morphology

was predominantly intergranular (IG) (90% or greater). The CGR during each test period was determined from the slope of the corrected crack length vs. time plots. For cyclic loading, only the rise time was used to determine growth rate. The crack extension during each test period was at least 10 times the resolution of the DC potential drop method, i.e., typically 5 μm. Thus, crack extensions were at least 50 μm.

However, for some specimens (e.g., from the V.C. Summer nozzle–to–pipe weld and butter alloys) the CGRs were extremely low, e.g., less than 1×10^{-11} m/s, and crack extensions were less than 50 μm even after test durations in excess of 200 h. Thus, in these specimens, in the direction of crack advance, the crack typically grew less than one grain in the allotted period of a few hundred hours. Nevertheless, along the full width of the sample, it was estimated that in each constant–load period, crack growth encountered ≈300 grain boundaries in WCR-01, where the crack front was along the columnar grains, and ≈45 grain boundaries in BCR-01, where the crack front was across the columnar grains. How well do these populations of boundaries describe the specimens was also analyzed, i.e., how representative are these populations of the full spectrum of boundary types in the sample – the grain boundary character distribution (GBCD). By employing a simple statistical formalism by Alexandreanu and Was[40], and assuming a random boundary fraction of 70%, which is typical for a weld alloy, the fractional errors for the fractions of (cracked) random boundaries was calculated to be approximately 3.8% for WCR-01 and approximately 9.7% for BCR-01. Both numbers are comparable with the degree of homogeneity of random boundaries in a Ni–alloy; thus, as far as GBCD is concerned, no additional benefit can be gained by considering larger populations of boundaries. Using the same approach, the benefit of doubling the testing time from 200 to 400 h was also evaluated. Assuming a similar CGR, the population of cracked boundaries in BCR-01, for example, would double to approximately 90 in each constant-load period. As a result, the possible error in the fraction of random boundaries would drop to 6.9%. These results were somewhat expected; for a class of boundaries as abundant as random boundaries are in weld alloys, the improvement in fractional errors obtained by increasing the sample size (i.e., doubling the number of boundaries) is relatively small. From a crack advance viewpoint, it appears unlikely that a change in the population of random boundaries of the order of 3% would significantly affect the observed cracking behavior of the material.

In the present study, because a modified configuration of disc–shaped CT specimen was used, the stress intensity factor range ΔK was calculated using the correlations for the disc–shaped specimen as follows:

$$\Delta K = \frac{\Delta P}{\left(B B_N W\right)^{1/2}} \frac{\left(2+\frac{a}{W}\right)}{\left(1-\frac{a}{W}\right)^{3/2}} f\left(\frac{a}{W}\right) \tag{8}$$

$$\Delta P = P_{max} - P_{min} \qquad \text{for } R > 0 \tag{9}$$

$$f\left(\frac{a}{W}\right) = 0.76 + 4.8\left(\frac{a}{W}\right) - 11.58\left(\frac{a}{W}\right)^2 + 11.43\left(\frac{a}{W}\right)^3 - 4.08\left(\frac{a}{W}\right)^4, \tag{10}$$

where P_{max} and P_{min} are maximum and minimum applied load, a is crack length, B is the specimen thickness, and B_N is the net specimen thickness (or distance between the roots of the side grooves).

The CGR results were validated in accordance with the specimen size criteria of ASTM E 1681 and E 647. These criteria are intended to ensure applicability and transferability of the cracking behavior of a component or specimen of a given thickness under a specific loading condition to a crack associated with a different geometry, thickness, and loading condition. The K/size criteria require that the plastic zone at the tip of a crack is small relative to the specimen geometry. For constant–load tests, ASTM E 1681 requires that

$$B_{eff} \text{ and } (W - a) \geq 2.5\,(K/\sigma_{ys})^2, \tag{11}$$

and for cyclic loading, ASTM 647 requires that

$$(W - a) \geq (4/\pi)\,(K/\sigma_{ys})^2, \tag{12}$$

where K is the applied stress intensity factor, and σ_{ys} is the yield stress of the material. In high–temperature water, because the primary mechanism for crack growth during continuous cycling is not mechanical fatigue, Eq. 11 is probably the more appropriate criterion, but Eq. 12 may give acceptable results. For high–strain hardening materials, i.e., materials with an ultimate–to–yield stress ratio $(\sigma_{ult}/\sigma_{ys}) \geq 1.3$, both criteria allow the use of the flow stress defined as $\sigma_f = (\sigma_{ult} + \sigma_{ys})/2$ rather than the yield stress. In the present study, the specimen size criterion was based on Eq. 12 and flow stress.

Under cyclic loading, the CGR (m/s) can be expressed as the superposition of the rate in air (mechanical fatigue) and the rates due to corrosion fatigue and SCC, given as

$$\dot{a}_{env} = \dot{a}_{air} + \dot{a}_{cf} + \dot{a}_{scc}\,. \tag{13}$$

During crack growth tests in high–temperature water, environmental enhancement of CGRs does not occur from the start of the test. Under more rapid cyclic loading, the crack growth is dominated by mechanical fatigue. The CGRs during precracking and initial periods of cyclic loading were primarily due to mechanical fatigue. In general, environmental enhancement is typically observed under loading conditions that would lead to CGRs less than 10^{-9} m/s in air, i.e., for K_{max} values of 15–20 MPa·m$^{1/2}$, load ratio R should be ≥0.5 and rise time ≥30 s.

This page is intentionally left blank.

3 Microstructural Characterization

3.1 Davis-Besse CRDM Nozzle and J–Groove Weld Alloys

Microstructural characterization of material from the nozzle and J–groove weld from Davis-Besse was conducted on planes matching those of cylindrical–tensile and CT specimens. The cross sections that were examined are along planes that correspond to axial and circumferential cracks (Fig. 18). The specimens were cut and mounted to show the microstructure on planes designated 03–1 and 03–2 in the Alloy 600 nozzle and 03–3 and 03–4 in the Alloy 182 J-groove weld. The specimens were mechanically polished with 1-µm diamond paste. The Alloy 600 specimens were etched with Marble's Reagent (hydrochloric acid, copper sulfate, and distilled water solution). The weld specimens were electrochemically etched in a 5% nital solution at 5 V at room temperature to show grain boundaries followed by etching in 70% phosphoric acid solution at 5 V to show the interdendritic microstructure.

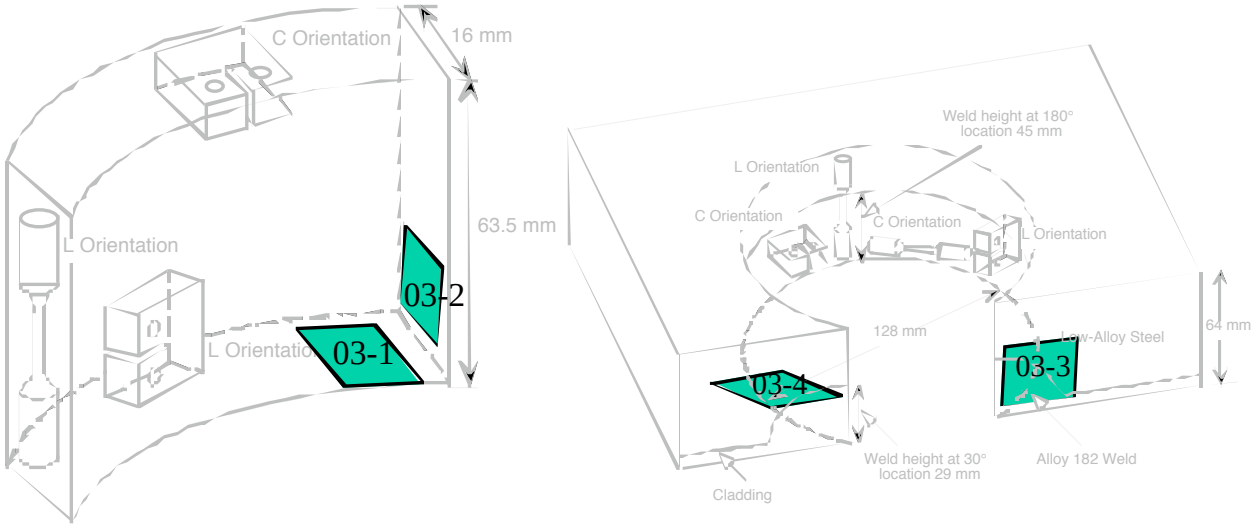

(a) (b)

Figure 18. Orientation of the planes on which metallography was conducted on material originating from Davis–Besse (a) CRDM Nozzle #3 and the (b) J–groove weld of Nozzle #11.

Figure 19 shows the microstructure observed along planes 03–1 and 03–2 of the Alloy 600 nozzle material; identical microstructure is observed for both planes. The grain size varies significantly, e.g., 30–200 µm, with an average size of ≈75 µm (ASTM grain size 4). Microhardness measurements indicated a uniform hardness across the nozzle wall. There is extensive grain boundary coverage (GBC) by Cr–rich carbides, and a few carbides are randomly distributed in the matrix. Although in most cases the boundaries are decorated with carbides, in some cases the carbides appear to be present only on one side of the boundary, e.g., the boundary going from top left to bottom right in Fig. 19d. The average size of the grain–boundary carbides was ≈0.3 µm, and the GBC was estimated to be in the range 50–60%.

Energy dispersive x–ray (EDX) analysis was performed to investigate the nature of the precipitates in the matrix and along the grain boundaries. The large precipitates in the grain matrix and boundaries were Ti rich. Figures 20a and b show micrographs of such precipitates. Figure 21 shows x-ray spectra obtained from the Alloy 600 background (matrix) and a Ti-rich matrix precipitate (Fig. 20a). The results are summarized in Table 6.

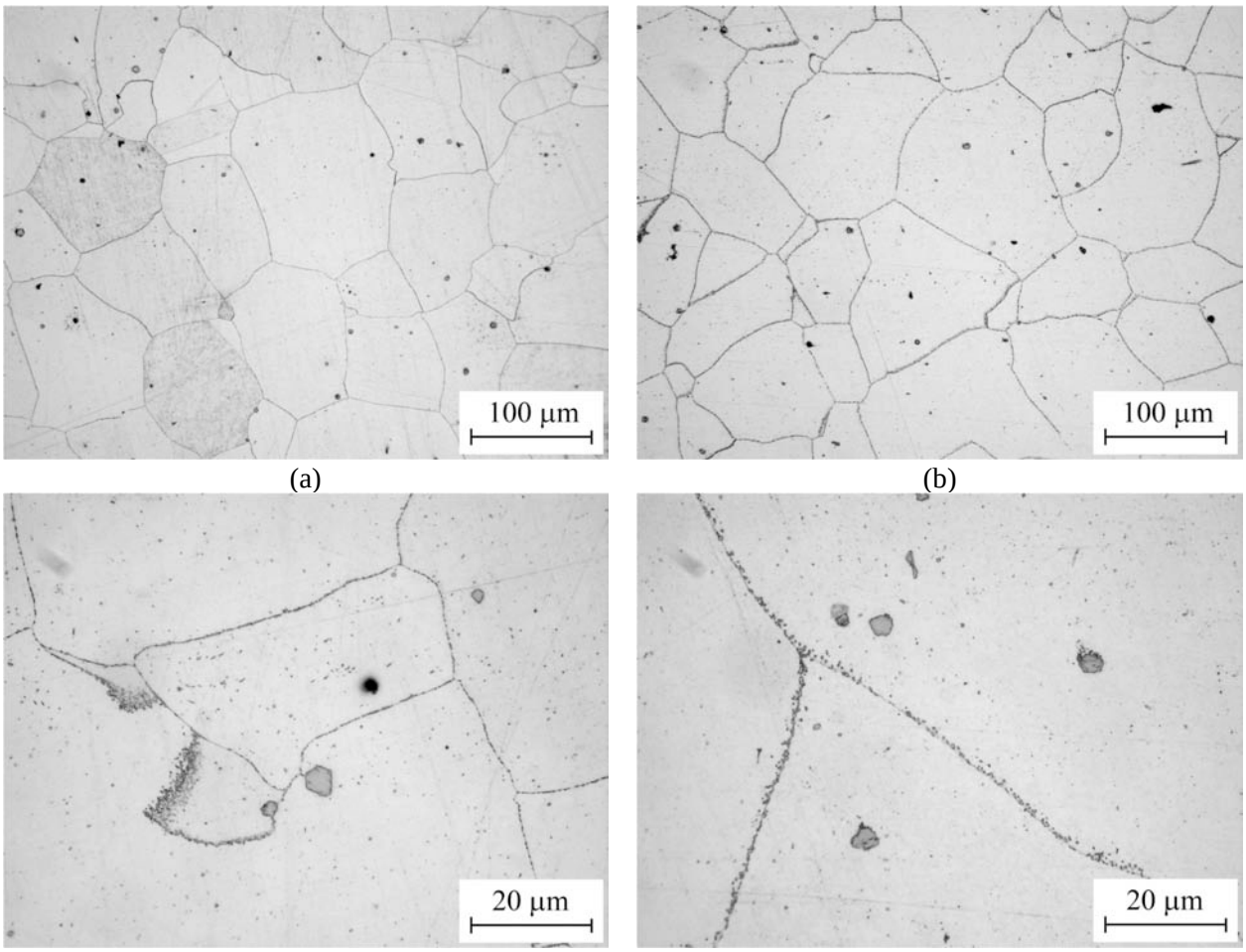

(a) (b)

(c) (d)

Figure 19. Microstructures observed on planes (a, c) 03-1 and (b, d) 03-2 of the CRDM nozzle alloy.

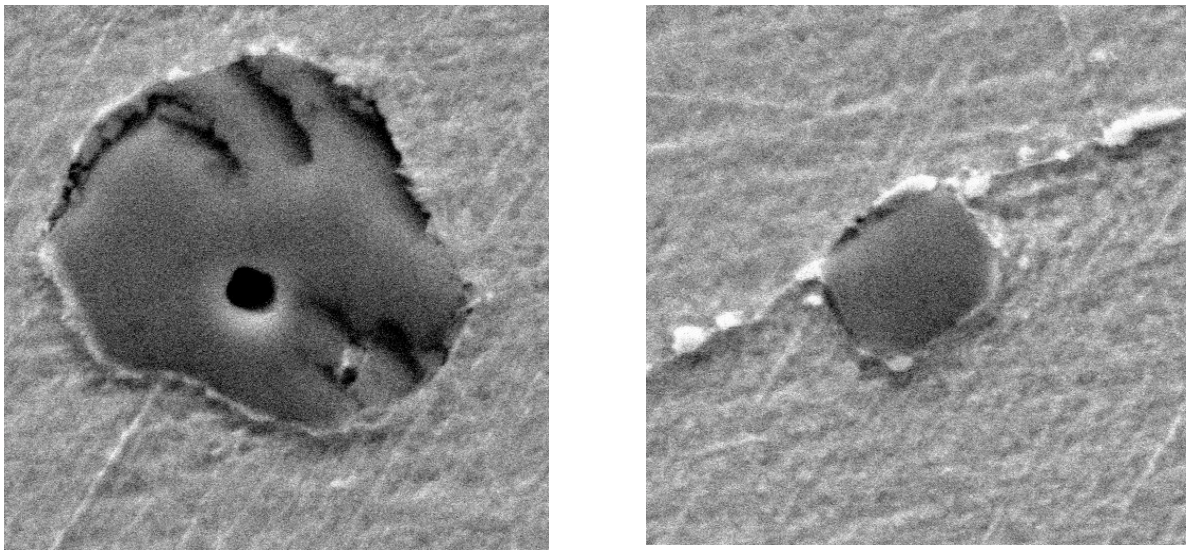

(a) (b)

Figure 20. Ti-rich precipitates observed in (a) the matrix and (b) grain boundary of the nozzle alloy.

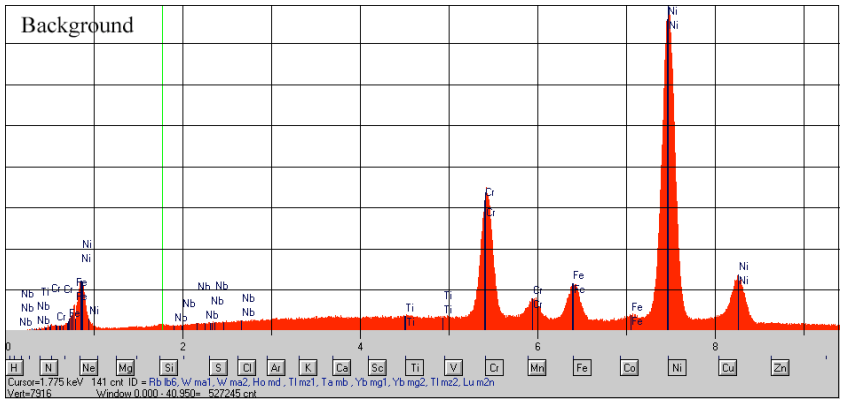

(a)

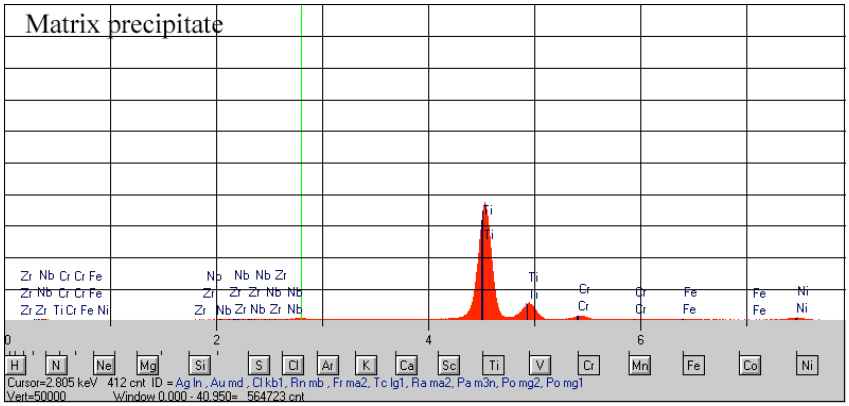

(b)

Figure 21. X-ray spectra obtained from (a) Alloy 600 bulk and (b) a Ti-rich matrix precipitate.

Table 6. Chemical composition of the bulk material and matrix precipitates obtained from EDX analyses of the Nozzle #3 Alloy 600.

	Element											
	Ni		Cr		Fe		**Ti**		Si		Nb	
	wt.%	at.%	wt.%	at.%	wt.%	at.%	wt.%	at.%	wt.%	at.%	wt.%	at.%
Background	79.57	77.80	14.20	15.68	5.39	5.34	0.27	0.32	0.21	0.44	0.27	0.17
Matrix precipitates	2.96	2.45	4.82	4.50	0.49	0.43	91.19	92.34	N/A	N/A	0.24	0.14

Figure 22 shows the microstructures observed on planes 03-3 (a, c, e) and 03-4 (b, d, f) of the J–groove weld alloy. These micrographs show the interdendritic microstructure typical of welds and are consistent with the relative orientation of the two planes of observation. Additional micrographs at higher magnification of the J–groove weld of CRDM nozzle #11 are shown in Fig. 23.

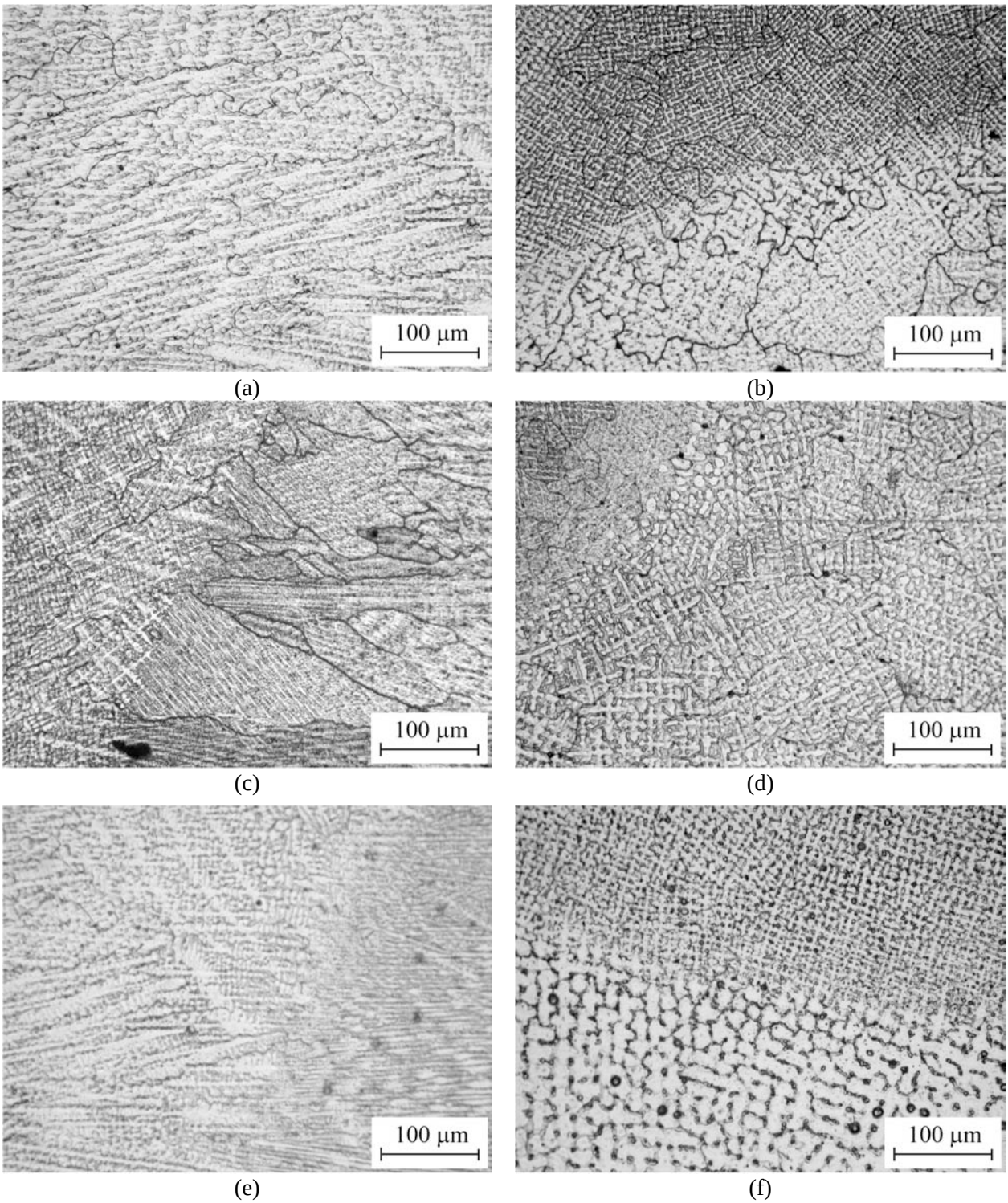

Figure 22. Microstructures observed on planes (a, c, e) 03-3 and (b, d, f) 03-4 of the J–groove weld alloy.

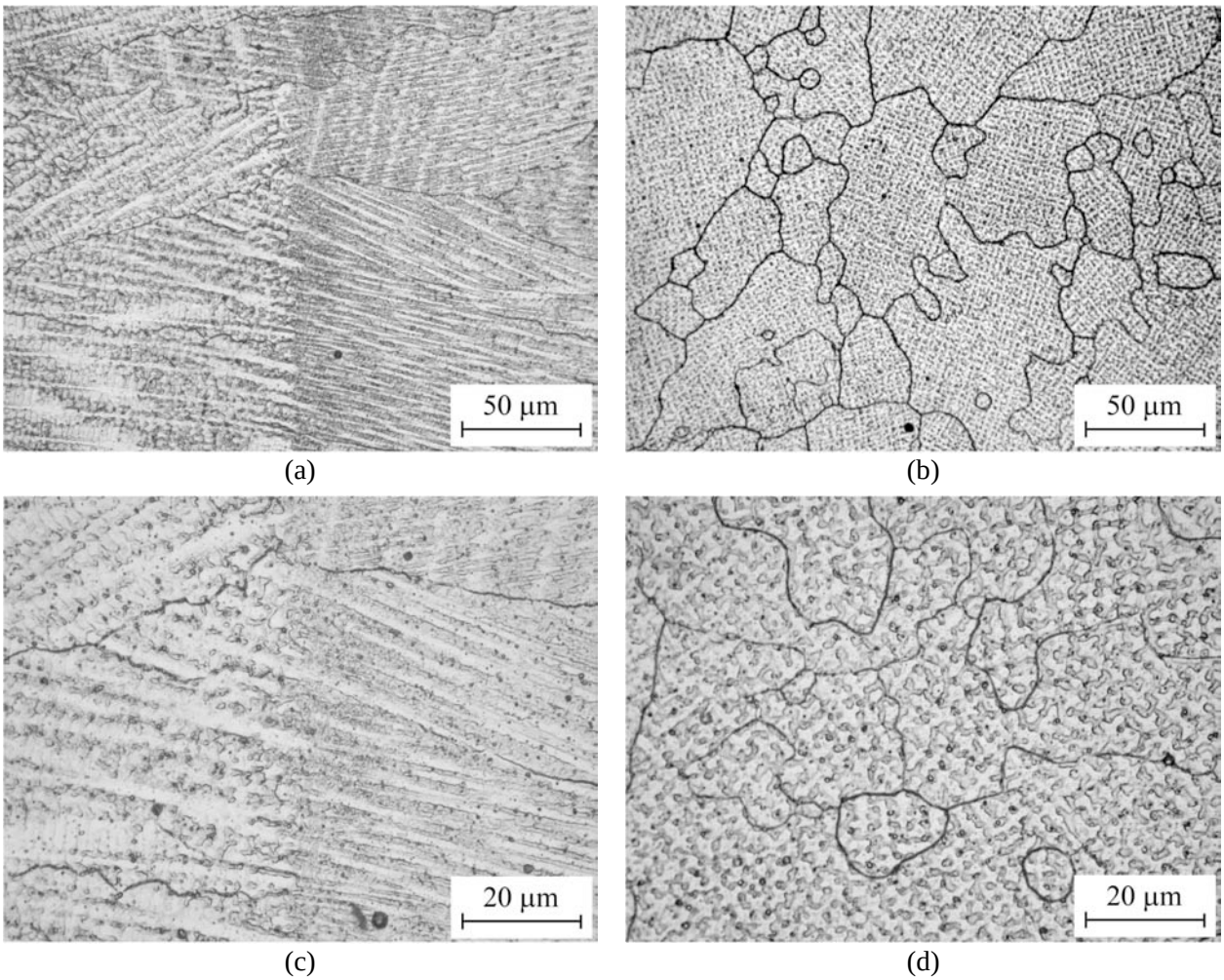

Figure 23. Higher magnification microstructures observed on planes (a, c) 03-3 and (b, d) 03-4 of the J–groove weld alloy.

Some microstructural characteristics of Ni–alloy weld metals, such as Alloys 182 and 82, are similar to those of wrought Alloys 600 and 690. Under certain thermal treatments, Cr–rich carbides can precipitate at both interdendrite and intradendrite grain boundaries.[41] Chromium depletion also occurs at the boundaries that are covered with such carbides. The precipitate phases are predominantly $M_{23}C_6$ and Ti–rich MC carbide. Nucleation of M_7C_3 carbides requires long periods at relatively high temperatures, whereas nucleation of $M_{23}C_6$ is quite rapid and cannot be avoided even during water quenching from solution treatment temperatures. Because of the rapid cooling of the weld metal from the fusion temperature, only $M_{23}C_6$ carbide precipitates during the welding process. The matrix also contains a uniform dispersion of the spherical γ' phase (Ni_3Ti).

The greater susceptibility of Alloy 182 to SCC as compared with Alloy 82 has been attributed to differences in Cr depletion because of differences in the composition of these two alloys. Alloy 182 contains higher concentrations of C and Fe and a lower concentration of Cr, all of which enhance Cr depletion during carbide precipitation.

Figure 24 shows the microstructure on plane 03-4 for the J–groove weld of the Nozzle #11. The micrographs show the interdendritic microstructure of the weld (a, b) as well as the presence of matrix

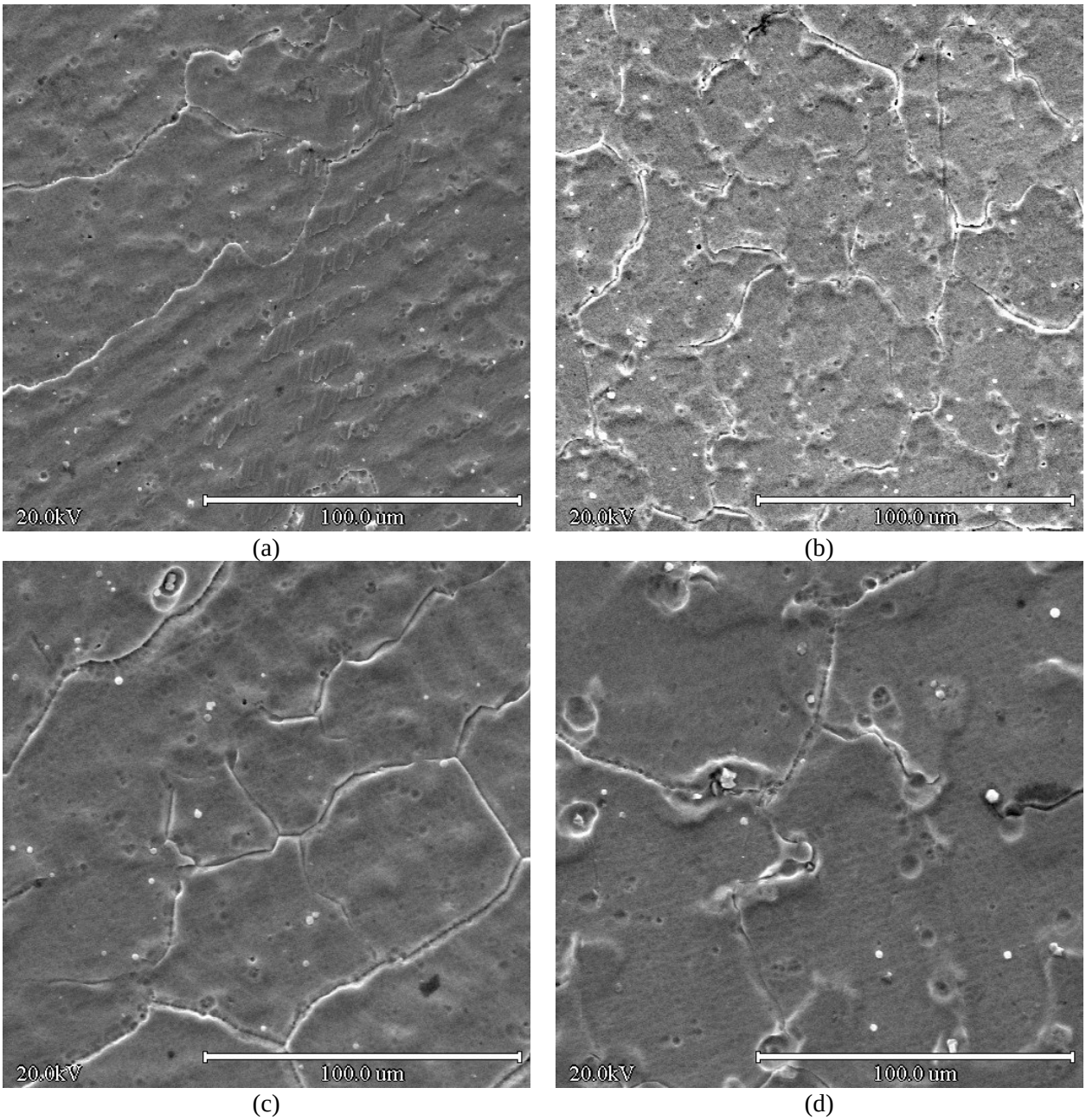

Figure 24. Microstructures observed on plane 03-4 for the J–groove weld of Nozzle #11.

and IG precipitates (c, d). Energy dispersive x–ray analyses were performed to investigate the nature of the precipitates in the weld alloy. The scanning electron microscope (SEM) micrograph in Fig. 25a shows the locations where X-ray spectra were collected. The graphs in Fig. 25 show the resulting spectra from background (positions 1 and 5, Figs. 25b and f), matrix precipitates (positions 2 and 4, Figs. 25c and e), and grain boundary precipitates (position 3, Fig. 25d). The resulting compositions are summarized in Table 7. The results indicate that matrix precipitates are Nb– or Si–rich, and that the grain boundary precipitates are Nb–rich.

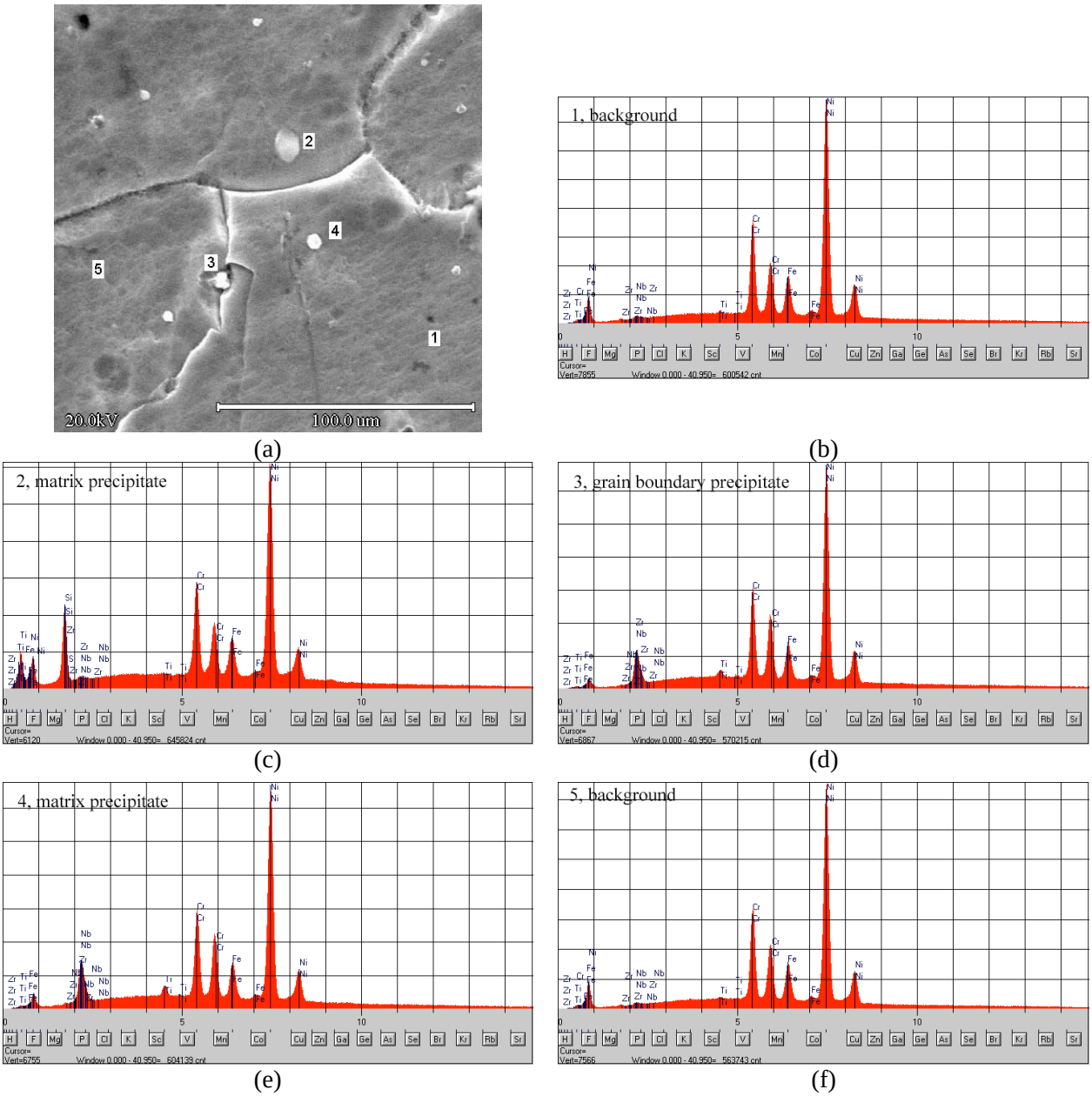

Figure 25. (a) Micrograph showing the locations where x-ray spectra were collected and spectra from (b) background, (c) matrix precipitate, (d) grain boundary precipitate, (e) another matrix precipitate, and (f) background at the completion of this series of analyses.

Table 7. Chemical compositions of the bulk material and matrix and grain boundary precipitates.

		Ni		Cr		Fe		Ti		Si		**Nb**	
		wt.%	at.%	wt.%	at.%	wt.%	at.%	wt.%	at.%	wt.%	at.%	wt.%	at.%
1	Background	75.85	74.38	14.70	16.28	7.96	8.21	0.35	0.42	N/A	N/A	1.12	0.69
2	Matrix precipitate	66.51	59.05	14.34	14.37	7.57	7.06	0.32	0.35	9.92	18.41	1.20	0.67
3	Grain boundary precipitate	67.84	68.92	13.68	15.69	6.93	7.40	0.95	1.19	N/A	N/A	10.58	6.79
4	Matrix precipitate.	65.85	67.47	13.14	15.20	6.81	7.34	1.30	1.64	N/A	N/A	12.87	8.33
5	Background	75.93	74.39	15.01	16.60	7.82	8.06	0.30	0.36	N/A	N/A	0.92	0.57

3.2 V.C. Summer Reactor Vessel Nozzle–to–Pipe Weld Alloys

Metallography was performed on planes representative of the crack growth planes in the cylindrical–tensile and CT specimens from the butter and weld alloys. The metallographic samples, which were approximately 20 × 20 × 10 mm (0.78 × 0.78 × 0.39 in.), were cut as shown in Fig. 26. The samples, numbered 1–6, were investigated by optical microscopy in the plane of the picture, or on the planes normal to the arrows in the figure. The samples were mechanically polished with 1–μm diamond paste, and electrochemically etched in a 70% phosphoric acid solution at 5 V at room temperature in order to observe the microstructure.

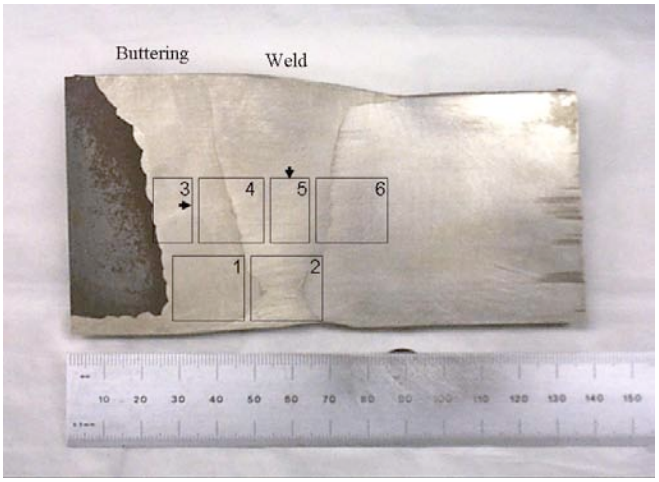

Figure 26.
Schematic showing the locations of the metallography samples cut from the V.C. Summer weld piece. All samples were investigated in the plane of the picture, unless indicated otherwise by arrows.

Figure 27 shows micrographs of the Alloy 182 butter microstructure (Sample #1) at increasing magnifications. The micrographs show interdendritic microstructures typical of welds and are consistent with the relative orientation of the two planes of observation: the elongated grains (and dendrites) are oriented primarily in a horizontal direction in Fig. 26. Figure 28 shows micrographs from Sample #3, with the observation plane indicated by the arrow in Fig. 26. The microstructure is typical of that generally observed along a plane perpendicular to the columnar grains and thus to the dendrites. A large defect can be seen in Fig. 28a, close to the boundary between two passes.

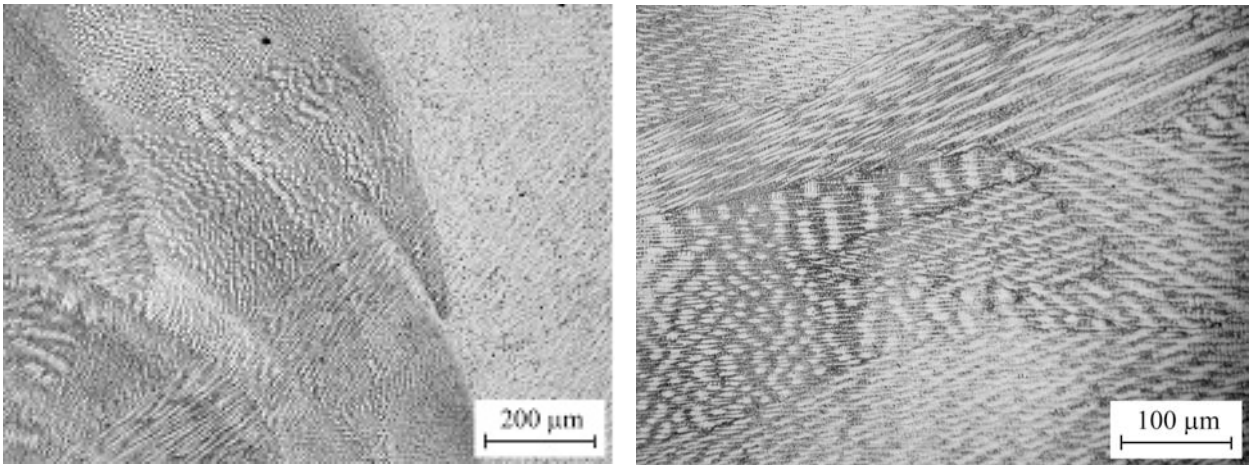

(a) (b)

Figure 27. Microstructure of the butter alloy in Sample #1.

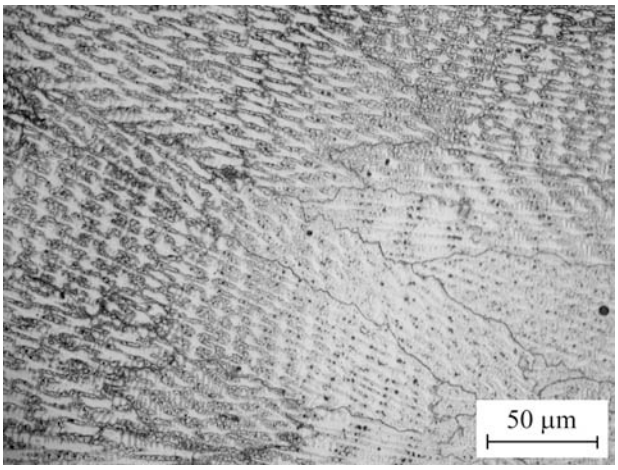

(c)

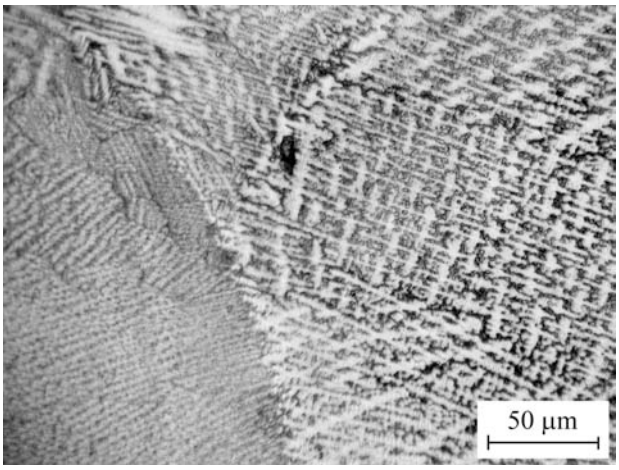

(d)

Figure 27. (Contd.)

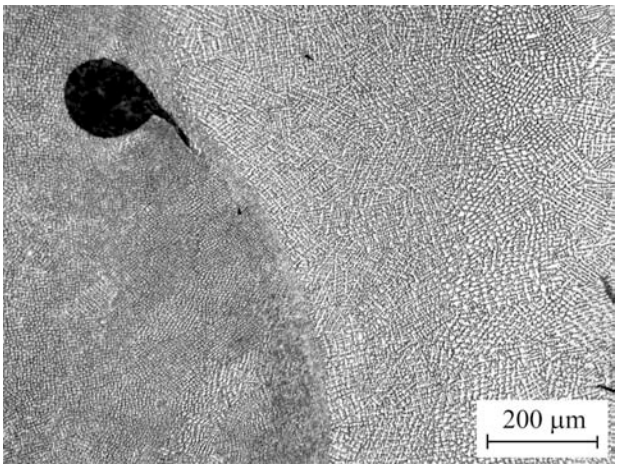

(a)

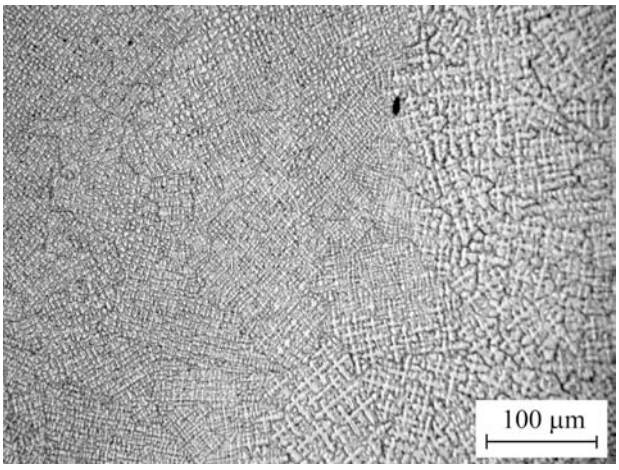

(b)

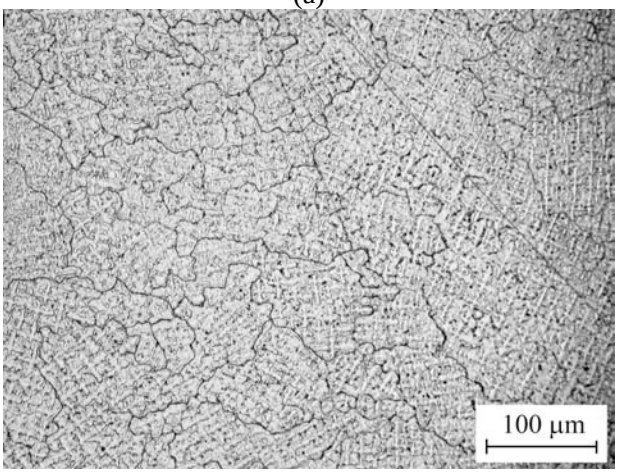

(c)

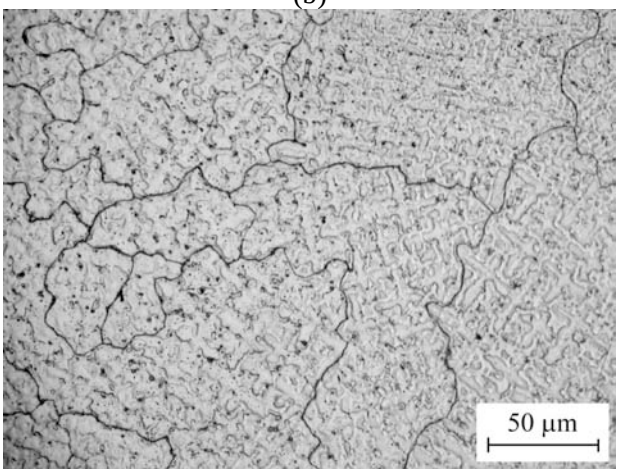

(d)

Figure 28. Microstructure of the butter alloy in Sample #3.

Figures 29 and 30 show the microstructure of the Alloy 182 weld. A typical weld microstructure was observed on Sample #2 (Fig. 29). The dendrites (and columnar grains) are oriented primarily vertically in the micrographs.

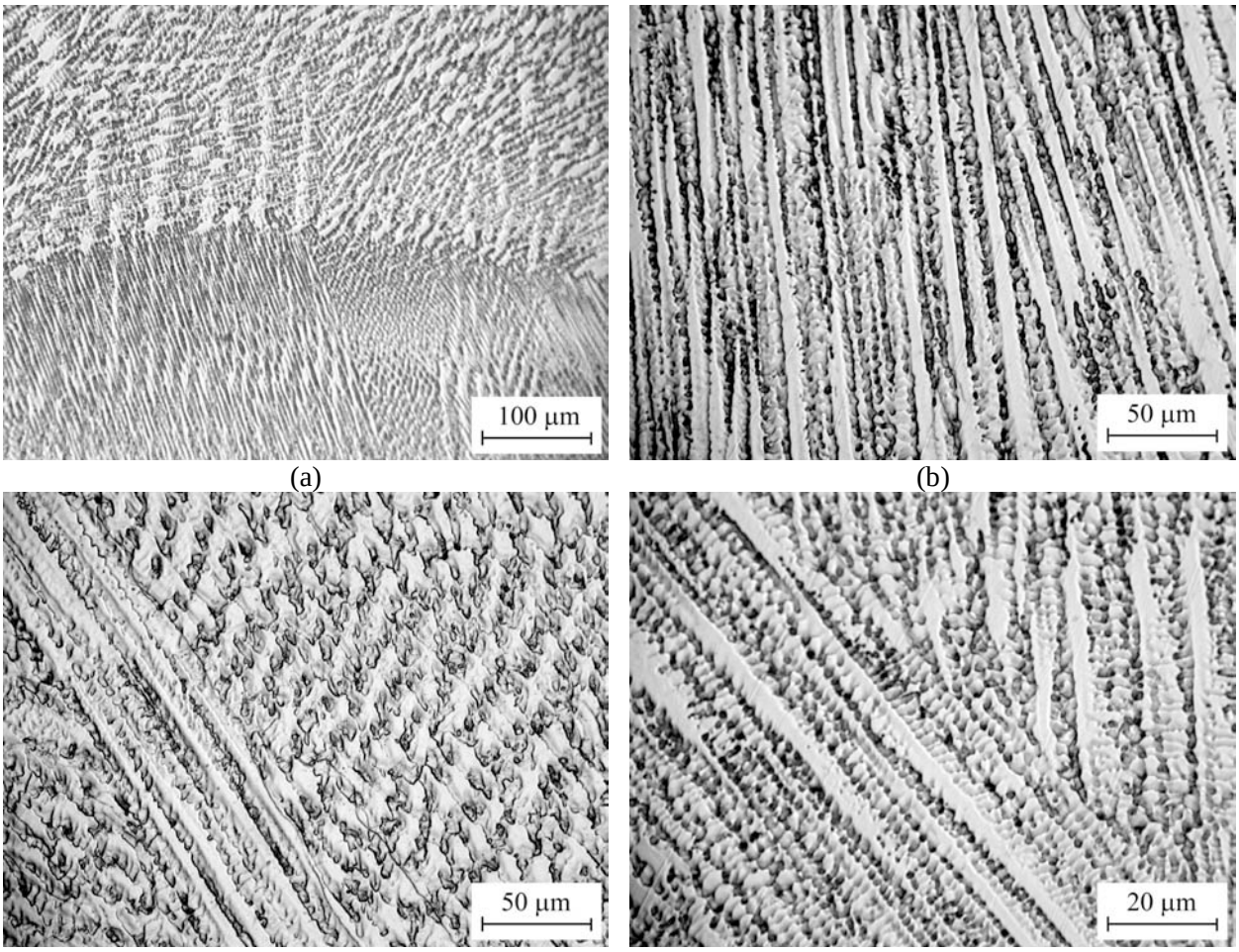

(a) (b)

(c) (d)

Figure 29. Microstructure of the weld alloy in Sample #2.

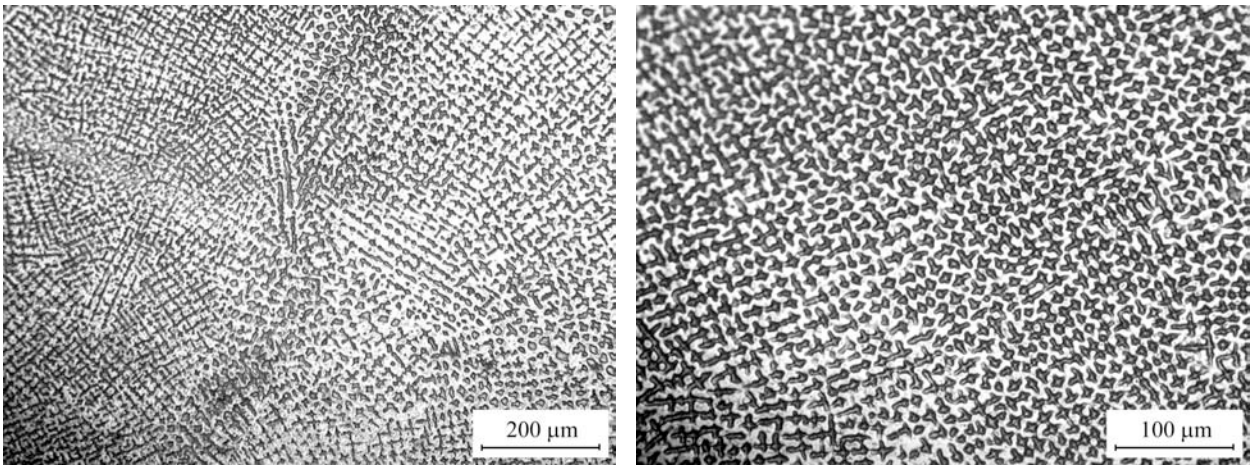

(a) (b)

Figure 30. Microstructure of the weld alloy in Sample #5.

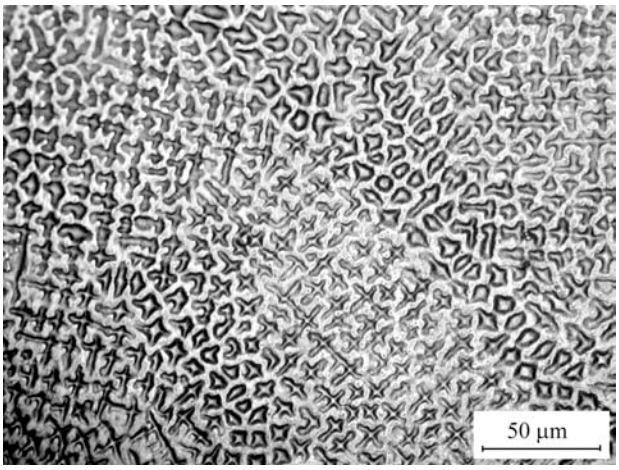

(c)

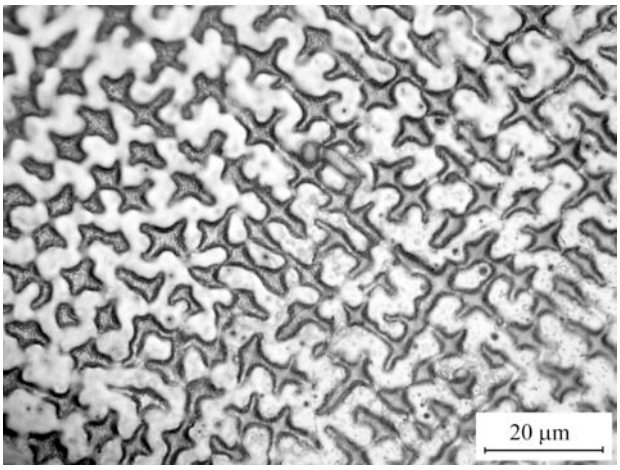

(d)

Figure 30. (Contd.)

Figure 30 shows the microstructure observed during examination of Sample #5, with the plane of observation indicated by an arrow in Fig. 26. As expected, these micrographs show an interdendritic microstructure typical of that generally observed along a plane perpendicular to the direction of dendrites. The butter-weld interface (Sample #4) is shown in Fig. 31. Typical weld–like dendritic microstructure are observed in both the weld and butter alloys.

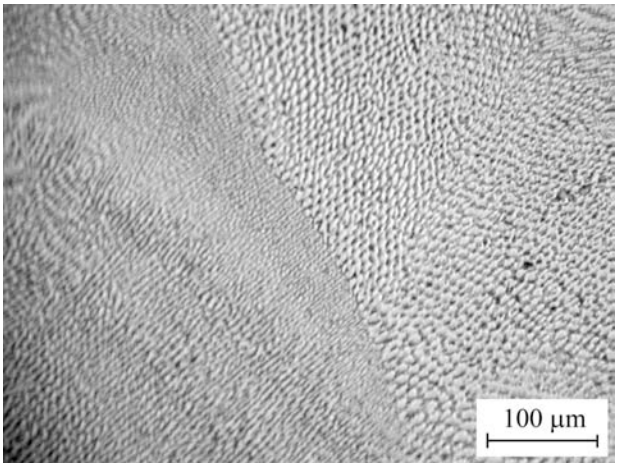

(a)

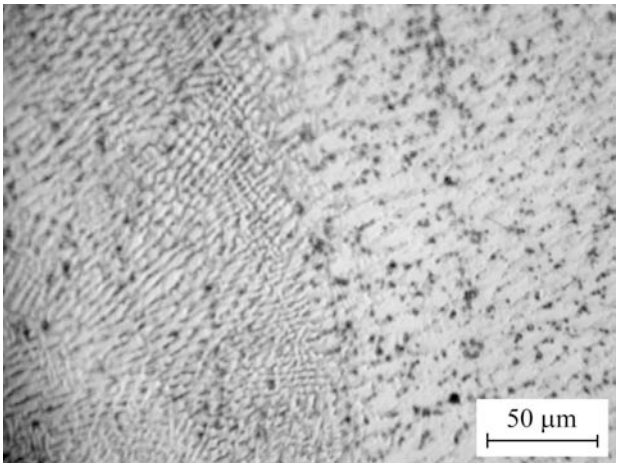

(b)

Figure 31. Microstructure of the interface between the butter and weld alloys in Sample #4.

The next two figures, Figs. 32 and 33, taken on Sample #2 in Fig. 26, are from a location away from where the actual CT specimens were cut; thus, the microstructural features revealed are unlikely to have any bearing on the SCC results presented in this report. Nevertheless, they offer some insight into the microstructure of a field weld previously subjected to repairs and, for that reason, are included in this section.

Micrographs revealing some of the defects observed in Sample #2 of the weld are shown in Fig. 32 at different magnifications. A high density of precipitates (Fig. 32a) of rather unusual appearance (Fig. 32b) can be observed throughout this region.

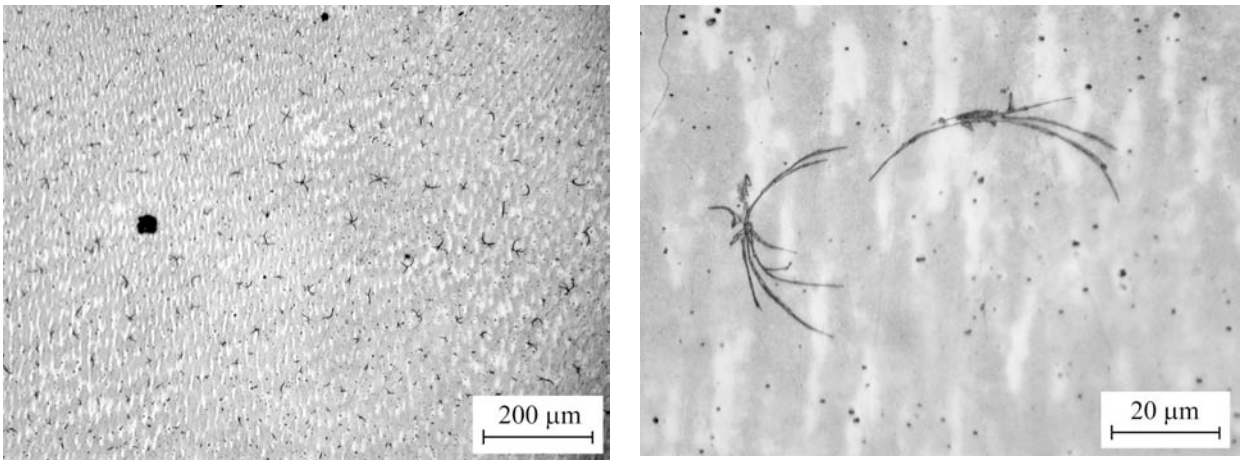

(a) (b)

Figure 32. Examples of defects in the weld alloy in Sample #2.

Of possible significance to the SCC behavior of this weld was the observation of grain boundary sliding at the interface between the Alloy 82 weld metal and the SS pipe. Several examples are indicated with white arrows in Fig. 33. Sliding occurred exclusively at grain boundaries (most likely high angle) extending from the pipe alloy to the weld alloy. Most likely, the grain boundary sliding occurred during the repair of this weld because of high residual stresses and local heating. Because grain boundary sliding is a precursor to intergranular stress corrosion cracking (IGSCC) initiation,[42] the interface appears to be very susceptible to SCC.

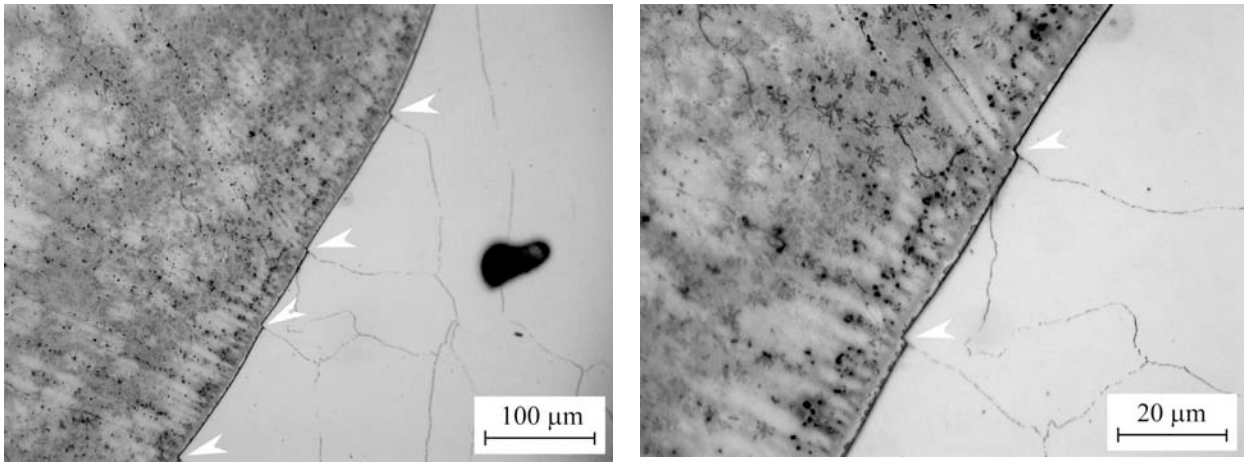

(a) (b)

Figure 33. Grain boundary sliding at the weld-pipe interface.